# The Eddy-Driven Jet and Storm-Track Responses to Boundary Layer Drag: Insights from an Idealized Dry GCM Study

CHEIKH O. MBENGUE AND TIM WOOLLINGS

*University of Oxford, Oxford, United Kingdom*

(Manuscript received 16 March 2018, in final form 30 November 2018)

ABSTRACT

Simulations using a dry, idealized general circulation model (GCM) are conducted to systematically investigate the eddy-driven jet's sensitivity to the location of boundary layer drag. Perturbations of boundary layer drag solely within the baroclinic zone reproduce the eddy-driven jet responses to global drag variations. The implications for current theories of eddy-driven jet shifts are discussed. Hemispherically asymmetric drag simulations in equinoctial and solstitial thermal conditions show that perturbations of surface drag in one hemisphere have negligible effects on the strength and latitude of the eddy-driven jet in the opposite hemisphere. Jet speed exhibits larger sensitivities to surface drag in perpetual winter simulations, while sensitivities in jet latitude are larger in perpetual summer simulations. Near-surface drag simulations with an Earthlike continental profile show how surface drag may facilitate tropical–extratropical teleconnections by modifying waveguides through changes in jet latitude. Longitudinally confined drag simulations demonstrate a novel mechanism for localizing storm tracks. A theoretical analysis is used to show that asymmetries in the Bernoulli function within the baroclinic zone are important for the eddy-driven jet latitude responses because they directly modulate the sensitivity of the zonal-mean zonal wind to drag in the boundary layer momentum balance. The simulations contained herein provide a rich array of case studies against which to test current theories of eddy-driven jet and storm-track shifts, and the results affirm the importance of correct, well-constrained locations and intensities of boundary layer drag in order to reduce jet and storm-track biases in climate and forecast models.

## 1. Introduction

Momentum mixing and dissipation play important roles in Earth's atmospheric energy cycle and momentum budget (Lorenz 1955; Phillips 1956). Early climate models used drag parameters to address biases in the models' climate (Stephenson 1994)—while drag parameters today are semiempirical and not well constrained. As a result, a body of research has developed around the impacts of subgrid-scale drag parameterizations on major features of the general circulation (James and Gray 1986; Stephenson 1994, 1995; Robinson 1997; Chen et al. 2007; Kidston and Vallis 2010; Sandu et al. 2016; Polichtchouk and Shepherd 2016; Pithan et al. 2016). One such feature is the eddy-driven jet.

Theoretical studies of the eddy-driven jet response to drag focused primarily on global drag variations (James and Gray 1986; Robinson 1997; Chen et al. 2007; Kidston and Vallis 2010; Polichtchouk and Shepherd 2016), although counterexamples exist; for example, variations in parameterized gravity wave (Stephenson 1994) and blocking drag are necessarily local because they depend on the variance of subgrid-scale orography.[1] These studies have shown that the eddy-driven jet shifts equatorward when gravity wave and near-surface drag are increased (James and Gray 1986; Stephenson 1994; Robinson 1997; Chen et al. 2007); while increases in hyperdiffusivity shift the jet poleward (Stephenson 1995), although questions remain about the dependence of this result on model resolution. A recent study has linked model biases to the quality and intensity of blocking drag parameterization and has called for improvements in low-level drag parameterizations in coarse-resolution climate models (Pithan et al. 2016).

Denotes content that is immediately available upon publication as open access.

*Corresponding author*: Cheikh Oumar Mbengue, c.mbengue@wolfson.oxon.org

[1] We do not consider the dynamics of resolved-scale orography.

DOI: 10.1175/JAS-D-18-0086.1

Their study highlights the need for regional idealized drag simulations to elucidate and refine current theories of eddy-driven jet shifts; this motivates the current study.

Several momentum sinks may exist in an atmosphere; however, here, we conduct simulations using a dry dynamical core and focus only on near-surface, boundary layer drag. We use dry, idealized simulations as a starting point for several reasons: 1) To determine the extent to which dry processes account for the eddy-driven jet's response to surface drag, 2) to isolate the impact of surface drag from changes in drag due to moist processes. For example, the latent heat release associated with moist convection in the tropics may increase the strength of the tropical overturning circulation, which increases the surface winds. Surface drag then acts to reduce those winds, which in turn modifies surface sensible and latent heat fluxes. 3) To remove the effect of drag on moist processes, like surface evaporation. 4) To reduce the incidence of simultaneous actors, which increases the chances of identifying causal relationships. We use quadratic drag and build upon previous work that used linear drag to understand the eddy-driven jet response to boundary layer drag in an idealized framework. Furthermore, we conduct numerous simulations over a wide quadratic drag parameter space.

There exist several proposed mechanisms for jet shifts in response to external forcing. One school of thought posits that changes in the spectral character of the extratropical eddies that converge momentum into the jet are primarily responsible for changes in jet latitude. For example, Chen et al. (2007) suggest that an increase in the eastward phase speed of baroclinic eddies that accompanies an increase in the speed of the eddy-driven jet shifts the jet poleward. But a comprehensive survey of the eddy-driven jet's sensitivity to localized Gaussian heating in the latitude–sigma plane (Baker et al. 2017) shows a range of forcing for which the jet shifts poleward even though the eddy-driven jet's speed decreases. Thus, an increase in the eastward phase speed of eddies does not always accompany poleward jet shifts, although it frequently does in idealized studies in response to common forcings (e.g., Robinson 1997; Chen et al. 2007; Barnes et al. 2010; Kidston and Vallis 2012; Lorenz 2014). To reconcile this apparent contradiction and building on the work of Kidston and Vallis (2012), Lorenz (2014) argued that a decrease in the eddy-driven jet speed could shift the eddy-driven jet poleward because lower phase-speed eddies are preferentially reflected poleward of the jet—instead of meeting and breaking at their critical latitude. This enhanced reflection implies reduced deceleration on the poleward side of the jet and a poleward shift or extension of the eddy-driven jet.

But another school of thought argues that changes in baroclinic driving initiate and maintain changes in the eddy-driven jet's speed and latitude. In midlatitudes, baroclinic eddies, the product of baroclinic instability (Charney 1947; Eady 1949), converge angular momentum into the jet and, in a statistically steady state, balance westerly momentum loss at the surface. Therefore, it is reasonable to expect this driving to exert dominant, first-order control on the characteristics of the eddy-driven jet. Several studies report changes in jet speed or latitude in response to changes in baroclinicity (e.g., Yin 2005; Brayshaw et al. 2008; Mbengue and Schneider 2017; Baker et al. 2017). In fact, some studies suggest that the changes in the spectral character of the eddies that accelerate the jet are, in fact, part of the effect of more fundamental causes, like changes in the jet or the baroclinicity itself (Barnes and Hartmann 2011; Baker et al. 2017; Mbengue and Schneider 2018). Yet still other studies suggest that the dynamics of barotropic instabilities and shears play an important role in jet responses (James and Gray 1986; James 1987).

Idealized simulations have proven useful in helping to disentangle simultaneous actors and to help establish and understand causal relationships. Here, we extend the work of previous authors on the storm-track and jet response to near-surface drag beyond global drag simulations to gain further insight. We suggest how the responses might relate to those in more complex models. Finally, we present a simple theory that explains the eddy-driven jet latitude response seen in our simulations. Section 2 follows with a description of the general circulation model (GCM) and the simulations conducted in this study. Section 3 presents the results and section 4 discusses them. Finally, concluding remarks are made in section 5.

## 2. Model and simulations

GFDL's Flexible Modeling System (FMS) is used to investigate the eddy-driven jet's response to perturbations in near-surface drag. The GCM is a three-dimensional, turbulent model, with a dry dynamical core and a set of dry physics schemes. The GCM solves the primitive equations on a sphere using a spectral transform method and is run at T42 spectral resolution. T85- and T127-resolution simulations were used to check the robustness of the results. The results are robust. The model has 30 unevenly distributed $\sigma$ levels ($\sigma = p/p_s$, where $p$ is pressure and $p_s$ is surface pressure).

Radiative fluxes are parameterized using Newtonian relaxation toward a prescribed, semigray radiative-equilibrium profile. The equilibrium profile is statically unstable in the lower troposphere (Schneider 2004). The profile is the same one used in Schneider and Walker (2006)

and Mbengue and Schneider (2013) in all but the solstitial-profile simulations, in which a new radiative-equilibrium surface temperature, which shifts the subsolar point off the equator, is defined as

$$T_s^e(\varphi) = \overline{T}_s^e + \Delta_h \left[\frac{1}{3} + 2\sin(\varphi_0)\sin\varphi - \sin^2\varphi\right], \quad (1)$$

where $\varphi$ is latitude, $\varphi_0$ is the latitude of the subsolar point, $T_s^e$ is the equilibrium surface temperature, and $\Delta_h$ is the pole-to-equator thermal contrast. The overline $\overline{(\cdot)}$ in Eq. (1) signifies a global mean. A quasi-equilibrium dry convection scheme, also described in Mbengue and Schneider (2013), relaxes temperatures within an atmospheric column toward a prescribed $6.9\,\mathrm{K\,km^{-1}}$ lapse rate in an energetically consistent way. The radiative forcing is constant throughout a given simulation: there are no diurnal or seasonal cycles. The surface is thermally insulated and has no topography.

Surface momentum transfer is modeled using quadratic skin friction. The drag coefficient is computed using Monin–Obukhov similarity theory. The default surface roughness is $5 \times 10^{-3}$ m, and the scheme uses a $1\,\mathrm{m\,s^{-1}}$ constant gustiness. A vertical diffusion parameterization diffuses dry static energy within a fixed-height, 2500-m planetary boundary layer. Horizontal $\nabla^8$ hyperdiffusion acts at the smallest resolved scales. All simulations are run for at least 1800 days. More complex configurations require longer integrations to attain a statistically steady state.

### a. The eddy-driven jet

In contrast to the subtropical jet, the eddy-driven jet is structurally barotropic. The mechanics of the eddy-driven jet differ from those of the subtropical jet: in the zonal mean, the eddy-driven jet owes its existence to baroclinic eddies, which converge angular momentum into midlatitudes to balance momentum loss at the surface. This convergence occurs primarily in the upper troposphere (Ait-Chaalal and Schneider 2015), but downward momentum transport through wave dynamics and residual, eddy-driven circulations barotropizes the jet, thus determining the surface winds. An equivalent barotropic structure of the extratropical jet emerges when meridional temperature gradients impose a vertical wind shear on the flow. Therefore, given the nature of the eddy-driven jet and following previous authors, near-surface winds are used as a proxy for the eddy-driven jet (Woollings et al. 2010). In this study, the term ''near surface'' refers to a vertical average between $\sigma = 0.8$ and $\sigma = 0.6$.

### b. Boundary layer drag parameterization

In addition to the skin-friction drag parameterization in the GCM, whose parameters are unperturbed, we add a quadratic drag parameterization, which retards the near-surface winds—a quadratic drag parameterization is an improvement over a linear, Rayleigh drag parameterization, which is common in idealized studies. The enhanced drag is given by

$$\frac{D\mathbf{V}}{Dt} = \cdots - C_D S(\varphi,\lambda,p)|\mathbf{V}|\mathbf{V}, \quad (2)$$

where $\mathbf{V}$ is the horizontal velocity vector, $|\mathbf{V}| = \sqrt{u^2 + v^2}$, where $u$ and $v$ are the eastward and northward components of the wind, $C_D$ is the quadratic drag coefficient, the parameter in this study, and $S(\varphi, \lambda, p)$ is a three-dimensional shape function that defines the spatial distribution of the boundary layer drag. The horizontal spatial coordinates $\varphi$ and $\lambda$ represent latitude and longitude. The boundary layer drag attains a maximum at the lowest grid level and decreases linearly to zero at the top of the boundary layer. In regions where the boundary layer drag is enhanced, it assumes a constant value in the horizontal plane. Note that ''no drag'' in this paper refers to no *enhanced* drag: all simulations have surface dissipation.

The radiation and convection parameterizations improve the tropical thermal stratification and the tropical tropopause height of the standard Held and Suarez (1994) configuration, which is really a benchmark for dry dynamical cores. Furthermore, our model does not have significant near-surface eddy temperature variances penetrating into deep tropics. Hence, tropical and extratropical dynamics interact in a more realistic way. Because we use a modern drag parameterization in concert with the aforementioned radiation and convection parameterizations, our simulations are the most realistic idealized, dry simulations to date to investigate the eddy-driven jet's response to near-surface drag.

### c. Covariance spectral analysis

To compute the northward temperature and momentum flux cospectra, the method of Hayashi (1971) is used. This method differentiates between forward- and rearward-propagating waves, and has found extensive use in the atmospheric science community (e.g., Randel and Held 1991; Chen et al. 2007). A 30-member, 90-day ensemble is used to compute the cospectra. The resultant four-dimensional output is a function of ensemble size, latitude, time, and longitude. Fourier transforms in time and longitude transform the model output into ensemble, latitude, frequency, and wavenumber. The frequency and wavenumber are converted to frequency and phase speed, $c = \omega a \cos\varphi / n$ (Randel and Held 1991), where $\omega$ is the frequency, $a$ is the planetary radius, $n$ is the wavenumber, and $\varphi$ is latitude. Summing over all wavenumbers and then taking the ensemble mean yields

model output that is a function of latitude and phase speed. The phase speeds are interpolated onto a $1\,\mathrm{m\,s^{-1}}$ resolution grid. In the plots of the phase-speed spectra, the control simulation represents an unperturbed simulation, while quadratic drag with a coefficient of $128 \times 10^{-7}\,\mathrm{m^{-1}}$ is added in the perturbed simulations. The large value ensures an easily detectable steady-state response.

### d. Continent-profile drag simulations

To compare and contrast changes in boundary layer friction over land versus over ocean, simulations are conducted in which boundary layer friction is modeled as

$$C_D = C_{D,O} \times \%H_2O + C_{D,L} \times (1 - \%H_2O), \quad (3)$$

where $C_{D,O}$ represents the drag coefficient over the ocean, $C_{D,L}$ represents the drag coefficient over the continents, and $\%H_2O$ is the faction of water covering a grid cell. Regions of sea ice are treated as ocean. Four simulations, which we refer to as continent-profile simulations, are conducted. Their drag distributions are detailed in Table 1.

### e. Zonally symmetric and hemispherically symmetric boundary layer drag simulations

Three groups of zonally symmetric boundary layer friction simulations are conducted. In one set of simulations—which follows previous studies—drag is varied globally and the changes in the speed and latitude of the eddy-driven jet are observed. In these global drag simulations, the drag coefficient $C_D$ is varied from $1 \times 10^{-7}$ to $1024 \times 10^{-7}\,\mathrm{m^{-1}}$. To separate the effects of global variations in drag from localized but zonally symmetric variations in drag, simulations are conducted in which drag is varied solely within the baroclinic zone. These simulations are referred to as baroclinic-zone drag simulations. The baroclinic zone is considered to be the constant-width regions between ±35° and ±55°N. The baroclinic-zone width is large enough that the eddy-driven jet maximum remains within the baroclinic zone over all simulations.

A set of zonally symmetric simulations, referred to as banded friction simulations, is conducted in which near-surface hemispherically symmetric drag is turned on progressively in 10° bands starting at the equator and moving poleward. The jet speed and latitude response are then observed. In these experiments, the drag coefficient where the friction is turned on is $200 \times 10^{-7}\,\mathrm{m^{-1}}$. A large drag coefficient is used in this experiment to ensure that the response is easy to identify.

### f. Zonally symmetric and hemispherically asymmetric boundary layer drag simulations

A novel set of simulations in which the drag coefficient is varied solely within one hemisphere and the jet response observed is also conducted. The Northern Hemisphere–Southern Hemisphere asymmetries on Earth make these simulations especially relevant. In these simulations, drag is varied from $5 \times 10^{-7}$ to $1200 \times 10^{-7}\,\mathrm{m^{-1}}$.

The last set of simulations shift the subsolar point 10° latitude into one hemisphere to mimic a winter and summer hemisphere. Then the drag is modified in one hemisphere and the eddy-driven jet speed and latitude responses are observed. These simulations elucidate the seasonal jet response to changes in near-surface drag.

TABLE 1. The enhanced drag coefficients ($10^{-7}\,\mathrm{m^{-1}}$) for the four continental-profile simulations. The letters "O" and "L" represent ocean and land, respectively.

| | Simulation name | | | |
|---|---|---|---|---|
| | No enhanced drag | Control | Oexp | Lexp |
| $C_{D,O}$ | 0.0 | 4.0 | 16.0 | 4.0 |
| $C_{D,L}$ | 0.0 | 32.0 | 32.0 | 44.0 |

## 3. Results

### a. Global drag simulations

The maximum zonal-mean jet speed decreases as boundary layer drag increases; see Fig. 1a. Changes in boundary layer quadratic drag over two orders of magnitude modifies the jet maximum over a range of about $5\,\mathrm{m\,s^{-1}}$. At high drag values, an increase in boundary layer drag slightly increases the jet speed (Fig. 1). The shape of the jet maximum curve is sigmoid-like when plotted on a log-linear axis; that is, the slopes of the curve at high and low values are modest compared to the center parts of the curve. As anticipated from the quadratic nature of the drag parameterization, the zonal-mean jet speed and latitude responses to boundary layer friction are nonlinear.

As the boundary layer drag increases, the jet shifts equatorward (Fig. 1b). This result agrees with previous idealized work, albeit with linear, Rayleigh drag, that shows an equatorward jet shift with increased drag. The jet latitude curve is also sigmoidal, but shows greater curvature when compared to the jet speed curve. The uncertainty is greater in the jet latitude response. The jet position has a 12° latitude range over the simulated drag parameter space.

### b. Meridionally asymmetric, zonally symmetric drag simulations

Boundary layer drag increasing solely within the baroclinic zone reduces the near-surface westerly wind maximum speed and shifts the eddy-driven jet equatorward (Figs. 2a,b). The baroclinic zone is the region of

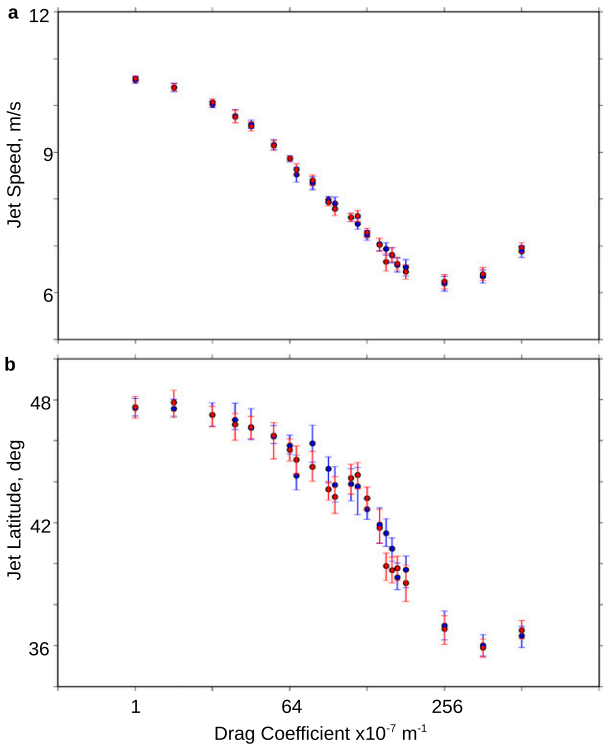


FIG. 1. The eddy-driven (a) jet speed and (b) jet latitude responses to global drag variations. The eddy-driven jet is measured using zonal-mean zonal winds averaged between $\sigma = 0.8$ and $\sigma = 0.6$. The blue dots indicate the Southern Hemisphere, while the red dots indicate the statistically independent Northern Hemisphere. The error bars show the 95% confidence interval about the jet's mean speed and latitude.

highest baroclinic activity. Here we assume it to be the region within ±35° and ±55°N. The baroclinic zone encloses the eddy-driven jet maximum in all simulations. The drag coefficient used in these baroclinic-zone simulations is $64 \times 10^{-7}\,\mathrm{m}^{-1}$.

Figure 2c shows the zonal-mean eddy-driven jet speed response to boundary layer drag that extends from the equator to the latitude specified on the abscissa; Fig. 2d shows the eddy-driven jet latitude response. The boundary layer friction is turned on in increments of 10° latitude in the direction of the black arrow in the figure. The blue dots show the jet in the Southern Hemisphere, while the red dots show the statistically independent jet in the Northern Hemisphere. Figure 2 shows that the eddy-driven jet abruptly slows and shifts equatorward when the drag reaches below the jet. The range of the change in jet speed and jet latitude is roughly the same as that for the global changes in boundary layer drag. For drag changes outside of the baroclinic zone, there is relatively little change in the jet except for an increase in jet speed when the boundary layer drag reaches the subtropics.

Figures 2c and 2d show that the greatest changes in the zonal-mean jet speed and position in response to near-surface drag perturbations occur when the drag extends into the baroclinic zone. The change is abrupt. As the drag extends into the subtropics, there is an increase in the near-surface westerly wind speed. As a rudimentary assessment of the statistical significance consider the agreement between the statistically independent hemispheres; that is, compare the blue dots to the red dots. However, as the jet extends further poleward, the near-surface wind maximum slows to its unperturbed value followed by an abrupt reduction upon entering and crossing the baroclinic zone. The jet responses are similar if the drag started from the pole and moved equatorward.

The zonal-mean zonal wind response to global changes in boundary layer drag is compared to changes in drag solely within the baroclinic zone in Fig. 3. The unperturbed simulation (Fig. 3) shows that the eddy-driven jet has a combined barotropic and baroclinic structure. The baroclinic part owes its existence to the north–south temperature gradient, while the barotropic component results from the action of extratropical eddies.

Global and baroclinic-zone simulations have a similar, barotropic reduction on the poleward flank of the jet. This suggests that there has been a reduction in eddy activity on the poleward flank of the jet. Furthermore, both simulations show a baroclinic reduction in the winds between 20°N and 20°S. The baroclinic nature suggests that it might be due to enhanced eddy momentum flux divergence within the subtropics (see Fig. 4). Finally, both simulations show slight barotropic increases in the jet on the equatorward flank of the eddy-driven jet at about 40°N and 40°S.

The global drag simulation shows a substantial equatorial response that is not seen in the baroclinic-zone simulation—the near-surface equatorial easterlies are substantially damped in the global drag simulation, while there is negligible change in the baroclinic-zone simulation. It appears that the reduction in the subtropical jet speed is stronger in the baroclinic-zone simulation. This likely occurs because there is more eddy momentum flux divergence from the subtropics in the global drag simulations (see Fig. 4). It is worth noting that while the easterlies are damped near the surface, the Hadley circulation above the boundary layer strengthens somewhat.

The global minus baroclinic-zone difference plot in Fig. 3 shows negligible extratropical barotropic differences, although the global drag simulation has a baroclinic component that is absent from the baroclinic-zone simulation. Nonetheless, Fig. 3 shows that the eddy-driven jet response to global variations in drag is primarily an

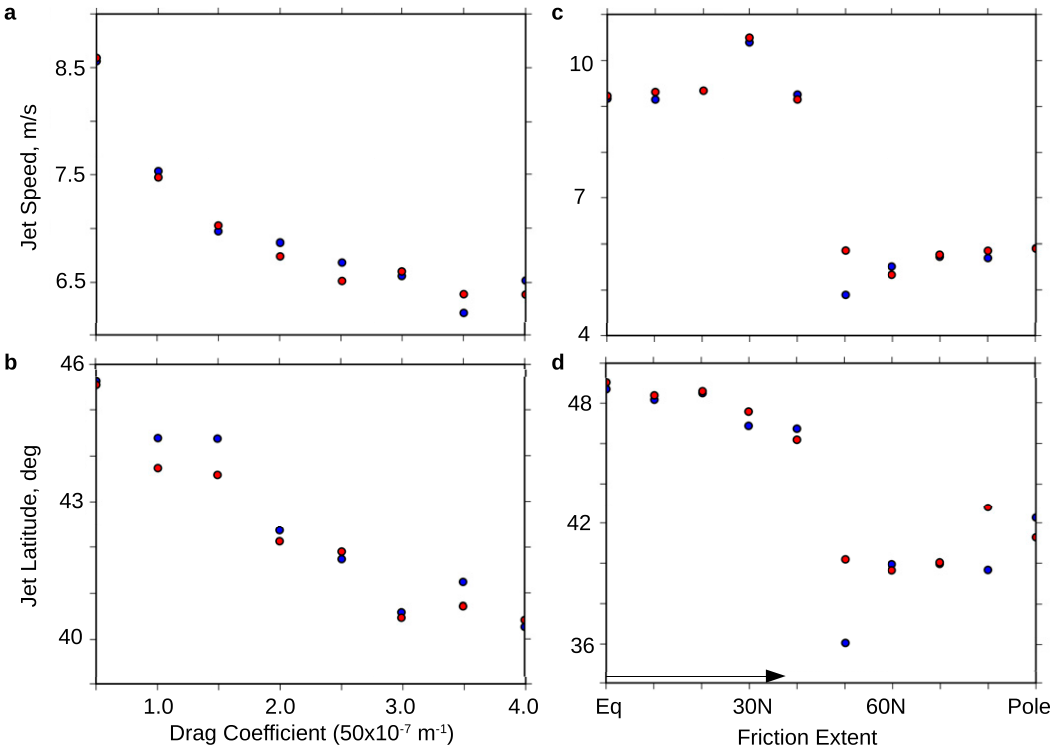


FIG. 2. The eddy-driven (a),(c) jet speed and (b),(d) jet latitude responses to boundary layer drag. (a),(b) Jet response to changes in boundary layer drag within the baroclinic zone, the constant-width region between 35° and 55°N/S. (c),(d) Jet response to near-surface drag that extends from the equator to the latitude specified on the abscissa. The eddy-driven jet is defined using the zonal-mean zonal winds averaged between $\sigma = 0.8$ and $\sigma = 0.6$. The blue dots indicate the Southern Hemisphere, while the red dots indicate the statistically independent Northern Hemisphere.

eddy-driven jet response to variations in drag in the baroclinic zone.

To help understand the differences between the global and baroclinic-zone simulations Fig. 4 and Fig. 5 show the eddy momentum flux divergence and the meridional eddy heat fluxes for the unperturbed, baroclinic-zone simulations minus the control, global simulations minus the control, and global minus the baroclinic-zone simulations.

Eddy momentum flux divergences on the flanks of the jet and eddy momentum flux convergence into the jet are higher in the global drag simulations. In both simulations, there is an increase in eddy momentum flux convergence equatorward of the maximum in eddy momentum flux convergence in the unperturbed simulation. The majority of the eddy momentum fluxes and the changes in them associated with the near-surface drag perturbations occur in the upper troposphere. Figure 4 shows enhanced eddy momentum flux divergence in the subtropics in both the global and baroclinic-zone simulations.

The reduction of the eddy meridional heat fluxes, which are associated with baroclinic driving, on the poleward side of the jet is evident in Fig. 5. This reduction occurs in both the global drag simulation and the baroclinic-zone drag simulation. The global versus baroclinic-zone difference plot shows that the reduction is identical to within $1\,\mathrm{K\,m\,s^{-1}}$ (Fig. 5). The largest differences in the eddy meridional heat fluxes between the global and baroclinic-zone simulations occur on the equatorward flank of the jet. Because the equatorward shift of the eddy-driven jet is similar between the global and the baroclinic-zone simulations, and because the shift results from a reduction on the poleward flank of the jet, it stands to reason that the mechanism of the eddy-driven jet shifts in response to changes in the near-surface drag is related to the suppression of baroclinic eddy driving on the poleward flank of the jet.

The upper-level (300 hPa) northward eddy momentum fluxes in the control simulation peak at about ±45°N (Fig. 6). Extratropical eddies with phase speeds between 10 and $15\,\mathrm{m\,s^{-1}}$ transport the most momentum poleward. The convergences associated with the momentum fluxes place the eddy-driven jet about 5° poleward of the latitude of maximum poleward eddy momentum flux. The near-surface (850 hPa) heat/temperature fluxes also peak

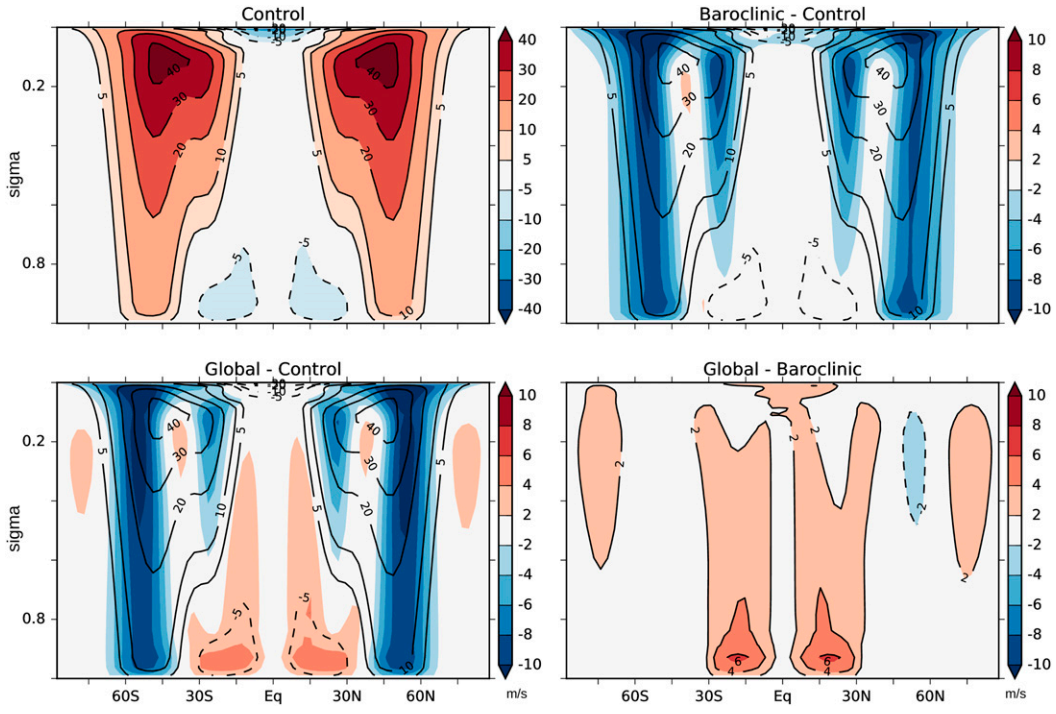


FIG. 3. The latitude–sigma zonal-mean zonal wind field for (top left) a control simulation with unperturbed near-surface drag, (bottom left) the globally enhanced near-surface drag simulation minus the control simulation, (top right) the enhanced near-surface drag within the baroclinic-zone simulation minus the control simulation, and (bottom right) the globally enhanced drag simulation minus drag enhanced within the baroclinic-zone simulation. The baroclinic zone is the axisymmetric region between ±35° and ±55°N. The black, unfilled contours, save for in the bottom-right panel, show the zonal-mean zonal wind field in the control simulation. The enhanced drag value used in the perturbed simulations is $64 \times 10^{-7}\,\mathrm{m}^{-1}$.

at about ±45°N, and eddies with phase speeds between 10 and 15 $\mathrm{m\,s}^{-1}$ also transport the most heat poleward (Fig. 7). The jet shifts equatorward when near-surface drag increases globally or within the baroclinic zone; however, the jet shift is greater when drag increases globally.

Figure 6 confirms that the eddy-driven jet shifts equatorward primarily because of reduced eddy momentum convergence on the poleward flank of the jet. Furthermore, all eddy phase speeds contribute to the reduction of momentum convergence on the poleward flank of the jet. Moreover, the subtropical critical lines do not shift equatorward. In fact, the critical line shifts in the opposite direction of the eddy-driven jet shift in the baroclinic-zone simulation, as shown by the thick green line. Hence, decreases in the eastward phase speed of equatorward-propagating eddies cannot explain the equatorward shift in our simulations. The critical line on the poleward flank of the jet shifts equatorward. Therefore, the critical line appears to respond to changes in eddy momentum flux divergences rather than constrain the eddies in a causal way.

The differences in eddy momentum fluxes between the global and baroclinic-zone simulations do not show any shifts to lower eddy phase speeds (Fig. 6). There is only an anomalous dipole centered on about 40°N, which implies anomalous convergence at 40°N. Therefore, another mechanism must explain the enhanced shift in the global drag simulation. This mechanism need only to explain the equatorward shift of the eddy momentum fluxes.

Figure 8 shows the responses of 1) eddy-driven jet speed and latitude, 2) the maximum eddy momentum fluxes in the upper troposphere, and 3) the poleward terminus of the Hadley cell[2] to increases in boundary layer drag solely in one hemisphere. In these simulations, the radiative forcing relaxes surface temperatures to an equinox meridional profile. The Hadley cell contracts under increases in near-surface drag. The circulation response occurs solely within the drag-modified hemisphere. The maximum eddy momentum

[2] The Hadley cell terminus is defined as the latitude of the first zero of the meridional streamfunction that is poleward of the maximum streamfunction, evaluated at the sigma level where the maximum occurs.

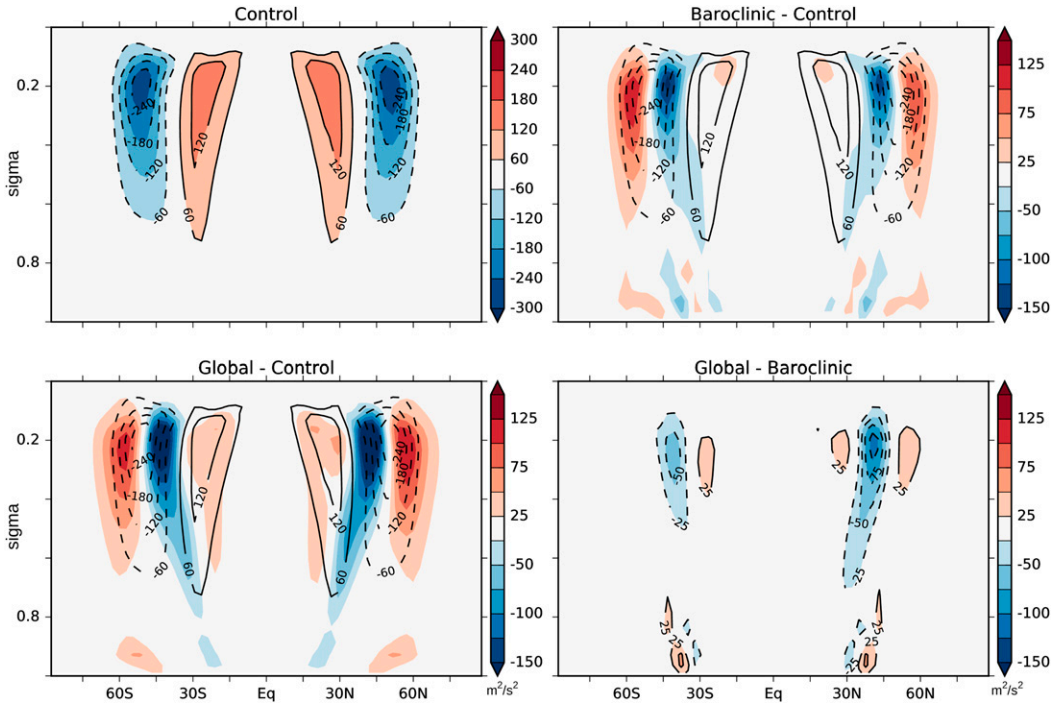


FIG. 4. The latitude–sigma eddy momentum flux divergence $\partial_\varphi(\overline{u'v'}\cos\varphi)/(R\cos\varphi)$ field for (top left) a control simulation with no enhanced near-surface drag, (bottom left) the globally enhanced near-surface drag simulation minus the control simulation, (top right) the near-surface drag enhanced in the baroclinic-zone simulation minus the control simulation, and (bottom right) the globally enhanced drag simulation minus the drag enhanced in the baroclinic-zone simulation. The baroclinic zone is the axisymmetric region between ±35° and ±55°N. The black, unfilled contours, save for in the bottom-right panel, show the field of eddy momentum flux divergence in the control simulation. We have multiplied by the constant radius of Earth to obtain units of $m^2\,s^{-2}$.

flux convergence reduces, which is consistent with a reduction in the eddy-driven jet speed.

Figure 9 shows the results of the asymmetric drag simulations with perpetual solstitial thermal profiles. Figure 9a shows the jet speed response, while Fig. 9b shows the jet latitude response. In the figure, the subscript "c" refers to control simulations, in which the boundary layer drag is unperturbed; while the subscript "p" refers to a perturbed simulation. The simulation $Eq_c$ is forced with a perpetual equinox thermal profile; $Eq_p$ refers to a simulation that is forced with a perpetual equinox thermal profile and within which the boundary layer drag in the Northern Hemisphere is increased. The simulation $So_c$ is forced with a perpetual solstice thermal profile. In contrast, $W_p$ and $S_p$, although also forced with perpetual solstitial thermal profiles, refer to simulations within which drag in the winter ($W_p$) and summer ($S_p$) hemispheres are enhanced compared to the opposite hemisphere.

Figure 9 shows that there is a greater shift in the jet latitude when near-surface drag is perturbed in the summer hemisphere. This may be because the summer jet is farther poleward compared to the winter jet, and thus it simply has more space to move. In addition, the fact that the summer jet is weaker and more susceptible to externally forced perturbations may also play a role. Interestingly, the magnitude of the decrease in the eddy-driven jet's speed is greater during the winter in comparison to the summer, yet the magnitude of the jet's equatorward shift in winter is smaller in comparison. The change in the magnitude of the eddy-driven jet is greater in winter because the magnitude of the unperturbed jet is stronger—since the meridional temperature gradients are stronger and because thermal wind balance implies a directly proportional relationship between the zonal-mean zonal wind shear and the zonal-mean meridional temperature gradient within an atmospheric layer. Furthermore, it can be shown that the change in the zonal-mean zonal wind $\Delta u_s = -0.5 u_s \Delta \ln C_D$, if the drag parameterization is quadratic, feedbacks are neglected, and eddy momentum flux convergences do not change appreciably. This results from a perturbation analysis of the steady-state, zonal-mean, vertically averaged zonal momentum equation, $\langle \partial_y \overline{u'v'} \rangle \approx C_D u_s^2$. Therefore, one can see explicitly that changes in the magnitude of the zonal-mean zonal surface winds in response to changes in boundary layer

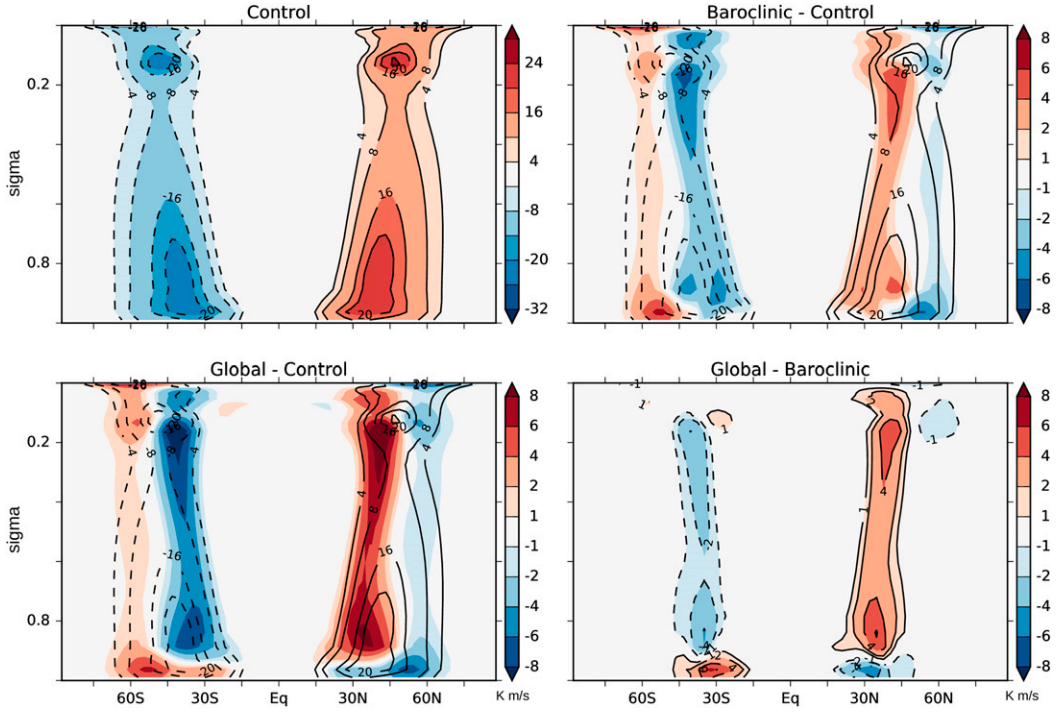


FIG. 5. The latitude–sigma meridional eddy heat fluxes $\overline{v'\theta'}$ field for (top left) a control simulation with no enhanced near-surface drag, (bottom left) the globally enhanced near-surface drag simulation minus the control simulation, (top right) the near-surface drag enhanced in the baroclinic-zone simulation minus the control simulation, and (bottom right) the globally enhanced drag simulation minus drag enhanced in the baroclinic-zone simulation. The baroclinic zone is the axisymmetric region between ±35° and ±55°N. The black, unfilled contours, save for in the bottom-right panel, show the field of eddy heat fluxes in the control simulation.

friction depend on the magnitude of the wind itself. Less well understood, however, is the reason that the magnitude of the equatorward shift in winter is smaller.

Figure 9 confirms that there are no appreciable interhemispheric communication of drag changes in one hemisphere to the eddy-driven jet and storm track in the opposite hemisphere.

### c. *Continent-profile drag simulations*

Figure 10a shows the near-surface westerly winds in the unperturbed, uniform drag simulation ($C_{D,L} = C_{D,O} = 0$). Because the simulation has no zonal asymmetries, the near-surface winds are zonally symmetric. Figure 10b shows the near-surface zonal wind response (the no enhanced drag simulation response has been subtracted) to an imposed horizontal profile of near-surface boundary layer drag in the shape of Earth's continents $C_{D,L} \neq C_{D,O}$. In this control simulation, the drag over the continents is greater than over the oceans (see Table 1). Under increases in boundary layer drag, the eddy-driven jets in both hemispheres shift equatorward. This is consistent with previous idealized experiments with globally perturbed drag. The equatorward shift in the Northern Hemisphere is greater because the near-surface drag change is greater. The jet response in the Southern Hemisphere is more zonally symmetric than in the Northern Hemisphere because there are fewer zonal asymmetries in the boundary layer drag profile in the Southern Hemisphere. Also, the figures suggest that idealized continental-profile boundary layer drag helps to establish localized jets in the Northern Hemisphere (the localized near-surface winds are seen better in the contours in Figs. 10c and 10d). However, in our idealized simulations, the localization of the eddy-driven jet is weak, as the low-level jet remains somewhat strong over the continents. Nonetheless, this result is consistent with previous work that used idealized continents in a more complex model (Brayshaw et al. 2009). In general, the eddy-driven jet speed decreases under regional increases in near-surface drag; however, regional jet speed increases are possible, as we show later. Southwest–northeast protrusions of westerly anomalies into the tropics become established off the west coasts of North America and Africa when boundary layer friction in the shape of the continents is introduced to a zonally symmetric friction profile.

Figure 10c increases the boundary layer drag over the oceans, while the drag over the land remains fixed at the

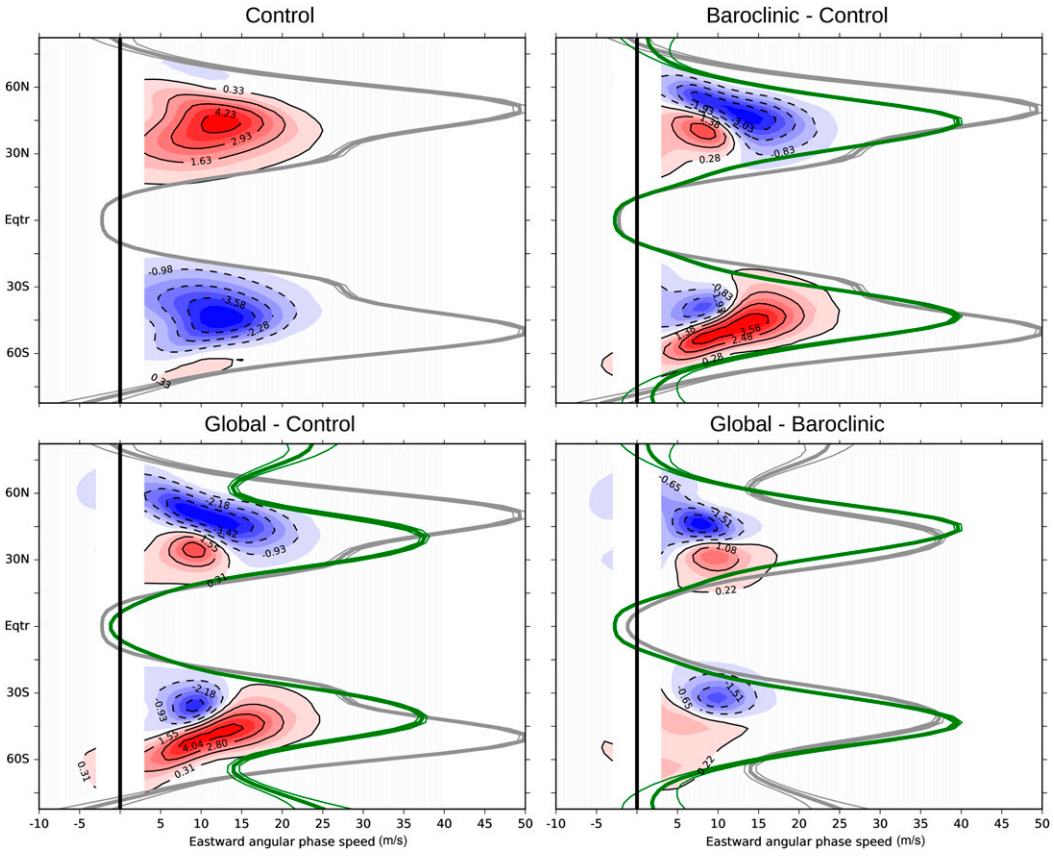


FIG. 6. The contours in the control simulation show the phase-speed spectrum of upper-level (300 hPa) northward momentum fluxes. The thick gray line in the control simulation shows the meridional profile of the upper-level westerly wind, which has been normalized by the cosine of latitude. The contours in the remaining plots show differences in the northward momentum fluxes. The thick green lines show the normalized westerly wind in the perturbed simulations. The thin lines bounding the westerlies are twice the standard error of a 30-member ensemble mean.

value used in the continental drag simulation (Fig. 10b). The contours show the climatological wind field from the simulation shown in Fig. 10b, while the color shading shows the difference from this. Figure 10c shows that jet responses are largest over the oceans and in the Southern Hemisphere. In the Southern Hemisphere, the jet shifts equatorward when the drag is increased; while in the Northern Hemisphere, the localized jets extend eastward and shift equatorward. In contrast, in Fig. 10d, in which the boundary layer friction is increased by the same amount but over the continents, the response in the Southern Hemisphere is less symmetric and weaker. Here, the Pacific jet shifts equatorward, but does not extend eastward. The Atlantic jet also shifts equatorward; however, it extends to the east on the southern flank as well. In contrast to the changes in boundary layer friction over oceans, the shifts in the jet that result from increases in friction over the land are concentrated on the western side of the Northern Hemisphere's ocean basins.

Figure 10d shows that the increase in boundary layer drag over the continents triggers a stationary-wave response that leads to a poleward shift of the jet stream over New Zealand, while an equatorward jet shift is seen to the west of South America. The eddy-driven jet's response to enhanced boundary layer friction over the oceans is annular mode–like, while it is stationary wave–like when perturbations are over the continents. In the Atlantic basin, the response to the perturbation to the ocean boundary layer drag has some features in common with the North Atlantic Oscillation.

The storm tracks, as represented by near-surface transient eddy meridional heat fluxes (Fig. 11), shift equatorward when the boundary layer drag is increased. Perturbations of drag over the oceans show an annular-mode-like response, while perturbations of drag over the land show a stationary-wave-like response. While perturbations of drag over the land cause a clear equatorward storm-track shift in the Northern Hemisphere, such a shift is not apparent in the Southern Hemisphere.

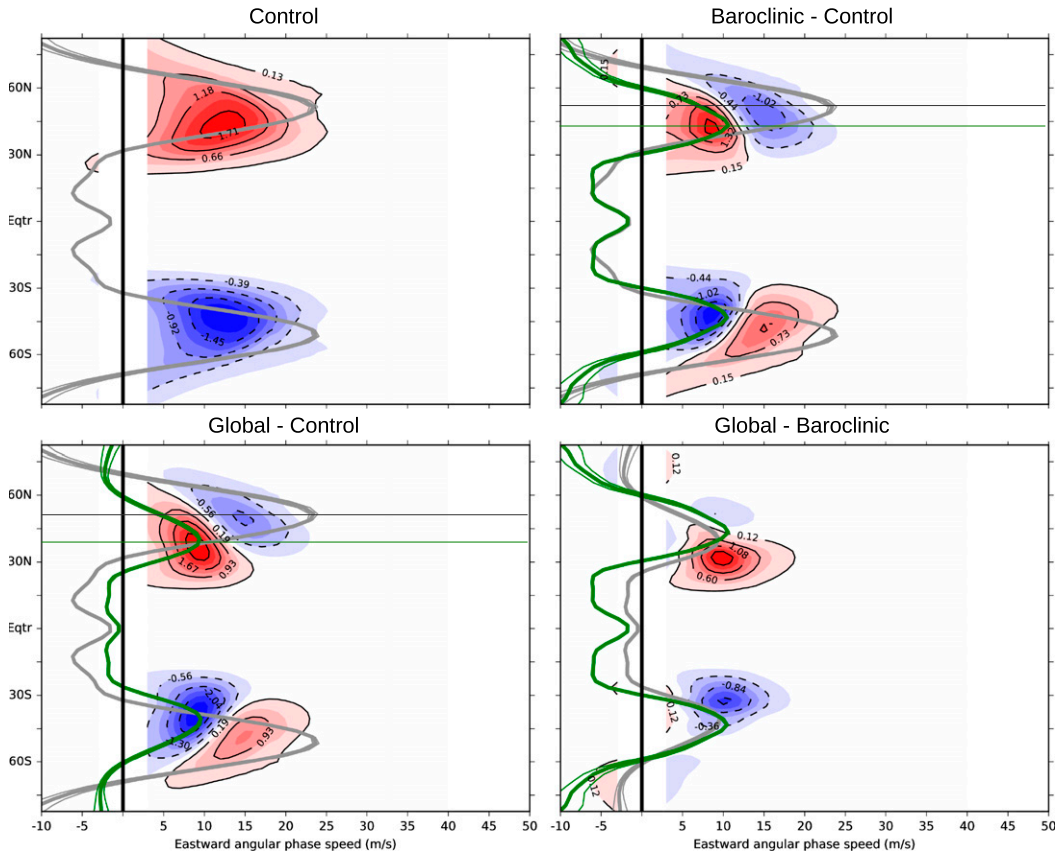


FIG. 7. The contours in the control simulation show the phase-speed spectrum of near-surface (850 hPa) northward temperature fluxes. (top left) The thick gray line shows the meridional profile of the near-surface westerly wind, which has been normalized by the cosine of latitude. (top right),(bottom left),(bottom right) The contours show differences in the northward temperature fluxes. The thick green lines show the normalized westerly wind in the perturbed simulations. The thin lines bounding the westerlies are twice the standard error of a 30-member ensemble mean. The thin horizontal lines mark the Northern Hemisphere westerly wind maximum.

Increasing drag over the ocean causes an equatorward storm-track shift irrespective of the hemisphere. The storm-track and eddy-driven jet shifts are in the same sense and with similar form (Fig. 10 and Fig. 11). This suggests that similar mechanisms might influence their responses.

Drag perturbations over the ocean result in north–south jet shifts downstream of the storm tracks (Fig. 10c), while perturbations over the land result in north–south jet shifts upstream of the storm tracks (Fig. 10d). To understand how localized drag perturbations impact the storm tracks, 10 simulations are conducted in which drag is perturbed in the baroclinic zone but in longitudinally confined regions that start at 0° and become progressively longer in longitude until the entire baroclinic zone is perturbed.

The jet axis, that is, the longitude profile of the maximum near-surface westerly winds, for simulations varying the longitudinal extent of the baroclinic-zone drag is shown in Fig. 12a. The latitude of maximum equatorward extent of the jet is a linear function of longitude until the longitude of the extent of drag reaches approximately 120°E, at which point the latitude of maximum equatorward extent ceases to be a function of longitude. A local maximum in equatorward extent, which is a linear function of the longitudinal extent of the baroclinic-zone drag, occurs at the downstream edge of the baroclinic-zone drag rectangle. The most poleward extent of the jet occurs around 10°E. In simulations of low drag extent, the maximum poleward extent of the jet is greater than the no-enhanced-drag case.

The longitude profile of the jet axis suggests that the localized near-surface drag, through its stationary response, exerts some control on the tilt of the jet. Figure 12a shows that the jet tilts equatorward with its most northerly extent at about 10°E and its most southerly extent at the smaller of two possible locations: 1) the easternmost edge of the near-surface drag and 2) 100°–120°E of the

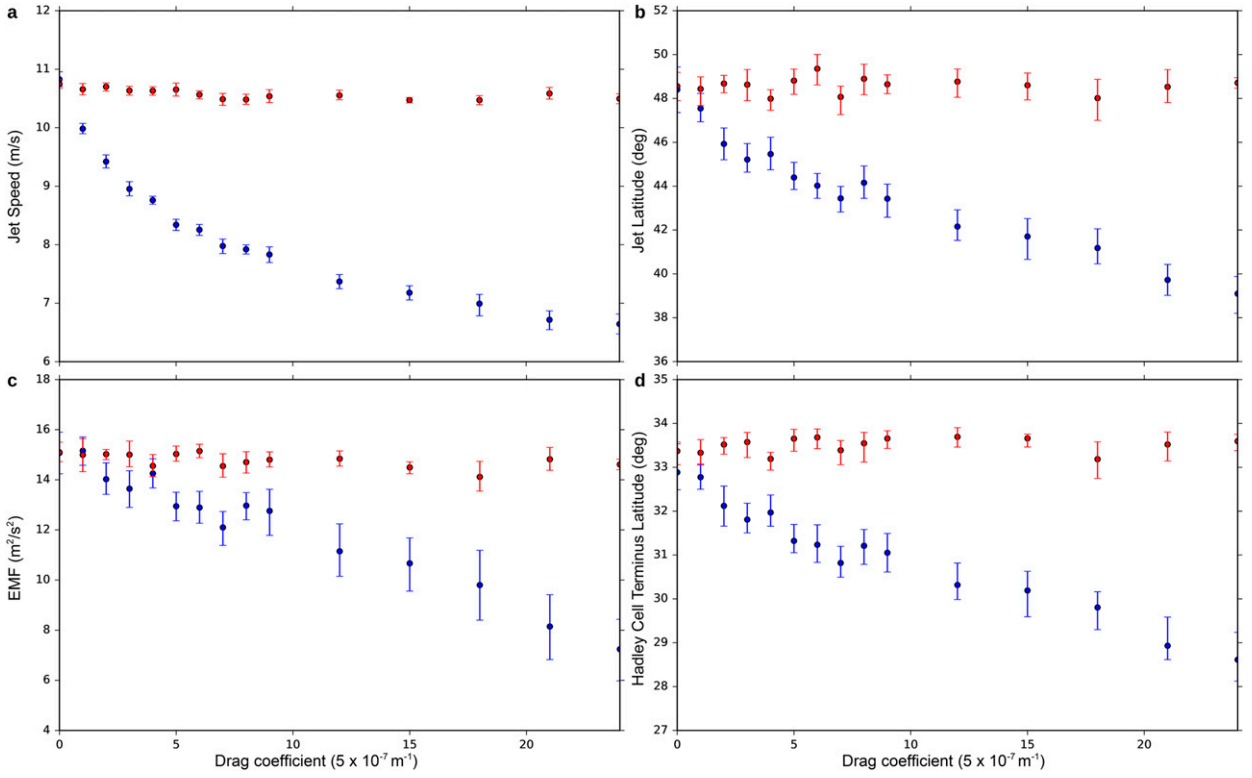


FIG. 8. (a) The jet speed, (b) the jet latitude, (c) the vertically averaged eddy momentum fluxes, and (d) the Hadley cell terminus latitude responses to variations in boundary layer drag in the Southern Hemisphere. The blue dots indicate values for the Southern Hemisphere, while the red dots indicate values for the Northern Hemisphere. The error bars are computed using a bootstrap procedure.

westernmost edge of the near-surface friction. If the baroclinic-zone drag extends beyond about 120°E, then there is a modest poleward tilt of the jet axis until the easternmost edge of the near-surface friction. The jet axis tilts strongly poleward, that is, a southwest–northeast tilt, east of the baroclinic-zone friction.

As the drag in the baroclinic zone extends eastward, the zonal-mean jet weakens (Figs. 12b,c) and shifts equatorward (Figs. 12c,d). The equatorward shift of the zonal-mean jet is a linear function of longitude despite the rich structure of the longitude profile of the near-surface westerly wind maximum. We find a 0.02° equatorward zonal-mean jet shift per 1° longitude of drag extent.

Figure 13 shows the jet speed along the jet axis. All perturbed jets attain their minimum magnitude within roughly one baroclinic-zone width east of the start of the baroclinic-zone drag. The longitude of this point appears independent of the drag extent. However, the jets all attain maximum values east of the imposed drag. The distance east of the drag that the jets attain the maximum appears to be a nonlinear, decreasing function of the drag extent.

The latitude–longitude field of near-surface westerly wind anomalies relative to the unperturbed simulation is shown in Fig. 14. A large portion of the jet shift is a reduction in jet speed on the poleward flank of the jet. The drag extent in each figure is represented by the dashed, magenta line. It is clear from the figure that the presence of the drag strip induces an equatorward jet shift in the vicinity of the drag. East of the enhanced drag, the response is tilted; hence, the presence of localized surface drag contributes to the jet tilt in localized storm tracks. These simple block continent experiments capture the north–south jet shifts downstream of the continents seen in the realistic continent-profile simulations (e.g., Figs. 10a,b in the Northern Hemisphere). This suggests that the details of the shape of the continents are secondary.

The storm-track response, as measured using near-surface transient eddy meridional temperature fluxes, is shown in Fig. 15. Poleward eddy temperature fluxes are enhanced downstream of the baroclinic-zone drag. The magnitude of the localized storm track increases as the extent of the drag increases. Within the enhanced-drag zone, eddy temperature fluxes shift equatorward, and show two maxima. This equatorward shift of the eddy temperature fluxes implies an equatorward shift of the baroclinic eddy activity. As the baroclinic stirring shifts equatorward, the zone into which upper-tropospheric

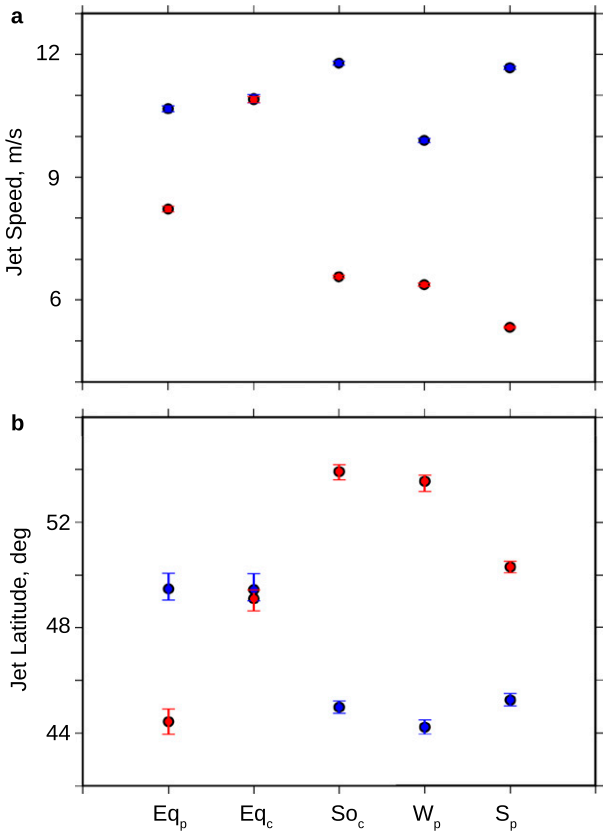


FIG. 9. (a) Jet speed and (b) jet latitude for three simulations in which boundary layer friction is perturbed, one unperturbed equinox control simulation ($Eq_c$), and one unperturbed solstice control simulation ($So_c$). $Eq_p$ shows jet speed and latitude for increased near-surface friction in the hemisphere indicated in red in an equinox profile, $W_p$ shows the two metrics for increased near-surface friction in the winter hemisphere, and $S_p$ shows the two metrics for increased near-surface friction for the summer hemisphere. In the solstice profile simulations, the blue dots indicate the winter hemisphere, while the red dots indicate the summer hemisphere. The error bars show the 95% confidence interval for the mean.

eddies converge momentum also shifts equatorward. Therefore, the eddy-driven jet also shifts equatorward.

Whereas the enhanced baroclinic-zone drag adds a tilt to an otherwise zonal jet, the induced storm track is zonal. Figure 16 demonstrates that stationary eddies help create and maintain the localized storm track. Note the induced favorable and adverse near-surface meridional temperature gradients downstream and upstream of the continent. That the stationary response helps maintain a localized storm track is not surprising as the localized storm track exists only in the zonally asymmetric simulations. However, it is also apparent from the figure that enhanced baroclinicity that is independent of induced stationary temperature gradients matters. The figure shows that the idealized continent excites a wave-1 stationary wave that depends on the longitudinal extent of the friction. The stationary wave is associated with a cyclone to the south of the continent and an anticyclone to the north. The net effect of the stationary-eddy fluxes is to steepen meridional temperature gradients on the eastern edge of the continent. The steepened temperature gradients then enhance transient eddy meridional temperature fluxes (i.e., the storm tracks) because meridional eddy temperature fluxes are a strong function of meridional temperature gradients.

## 4. Discussion

The global drag simulations, which cover two orders of magnitude of boundary layer drag changes, show that the eddy-driven jet shifts equatorward when boundary layer drag is increased. This agrees with previous idealized studies (Robinson 1997; Chen et al. 2007) and studies using more complex models (Polichtchouk and Shepherd 2016).

Near-surface westerly wind speed increases slightly when boundary layer drag is increased at high values of drag (Fig. 1a). Although slight, the increase is statistically significant. The mechanism of the increase can be understood using the theory of Robinson (2000). First, it has been established that the near-surface winds are maintained by eddy convergences of westerly momentum in the upper troposphere. This convergence occurs into regions where the eddies are generated, that is, into their source regions. In the GCM and as found on Earth, extratropical, synoptic-scale eddies are primarily of baroclinic origin. Changes in baroclinicity modify the eddy source region and, by extension, the region over which they converge momentum. A strong control of baroclinicity is the meridional temperature gradient, which is related to the vertical wind shear through thermal wind balance. Increases in near-surface drag reduces near-surface winds to first order. In the absence of compensating upper-tropospheric wind changes, this leads to an increase in the vertical wind shear, which, under the right condition, leads to additional baroclinic eddy activity, enhanced eddy momentum flux convergence, and an acceleration of the near-surface winds.

As near-surface drag enters the subtropics, the near-surface westerly wind maximum increases (Fig. 2c). Although several possibilities exist to explain this increase in maximum wind speed, we believe that the increase results from anomalous eddy momentum flux convergences in the upper troposphere driven by anomalous eddy driving associated with the edge of the friction impinging on the edge of the jet. In this context, the anomalous eddy activity may result from barotropic instability or from the north–south gradient in boundary layer friction interacting with the background winds.

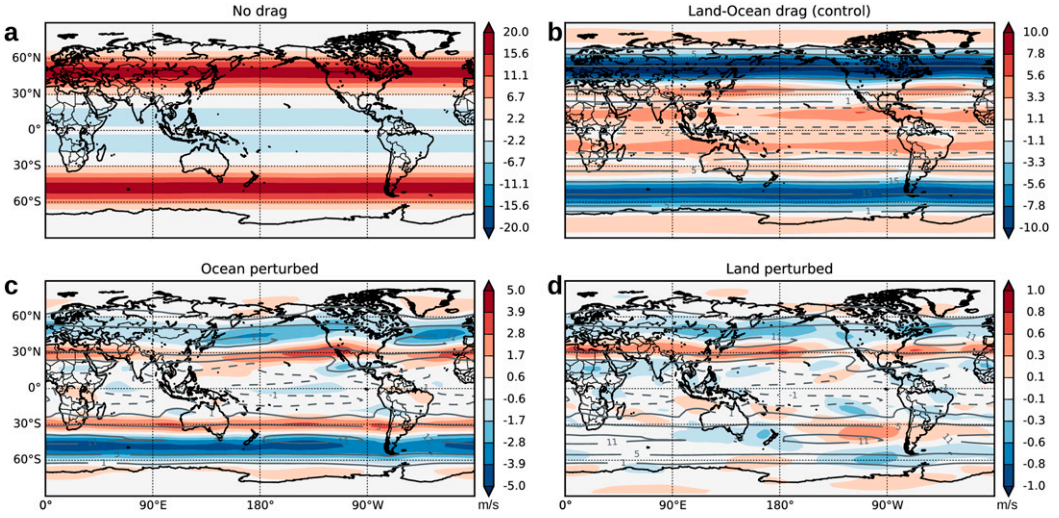


FIG. 10. Near-surface zonal wind response to variations in boundary layer drag. (a) Near-surface zonal winds in the no enhanced-drag simulation. (b) The Earthlike boundary layer drag simulation minus the no-enhanced-drag simulation (filled colored contours) and the near-surface zonal winds from the no-enhanced-drag simulation (gray unfilled contours). (c) Enhanced drag over the oceans simulation minus the Earthlike boundary layer drag simulation (filled colored contours) and the near-surface zonal winds from the Earthlike boundary layer drag simulation (gray unfilled contours). (d) Enhanced drag over the land simulation minus the Earthlike boundary layer drag simulation (filled colored contours) and the near-surface zonal winds from the Earthlike boundary layer drag simulation (gray unfilled contours).

That the increase in jet speed vanishes as the extent of the surface drag moves further poleward serves as evidence that the increase is edge related.

Comparing the global and baroclinic zone drag simulations, Fig. 3 shows that the response of the eddy-driven jet to global increases in drag are captured by varying drag solely in the baroclinic zone. Global variations of drag introduces additional responses that appear confined to the equatorial and polar regions, for the most part. Therefore, in addressing model biases in the eddy-driven jet, particular attention should be paid to drag parameterizations in the vicinity of the jet itself.

It is clear from Fig. 3 that the jet shift results from a barotropic reduction of the zonal winds on the poleward side of the eddy-driven jet. This implies a reduction in the eddy momentum flux convergence in that region.

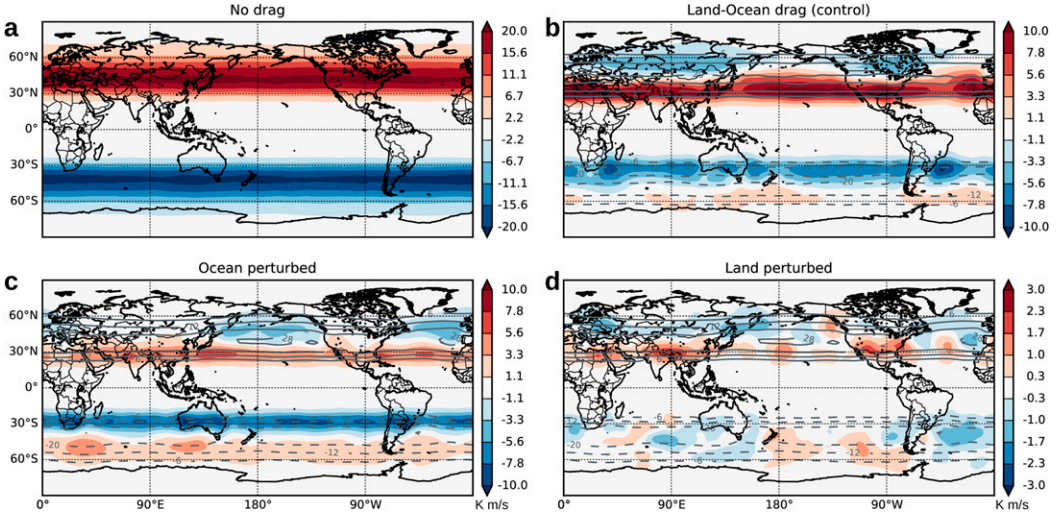


FIG. 11. As in Fig. 10, but for the storm-track response to variations in boundary layer drag. The storm track is identified using near-surface meridional eddy heat fluxes ($\overline{v'\theta'}$).

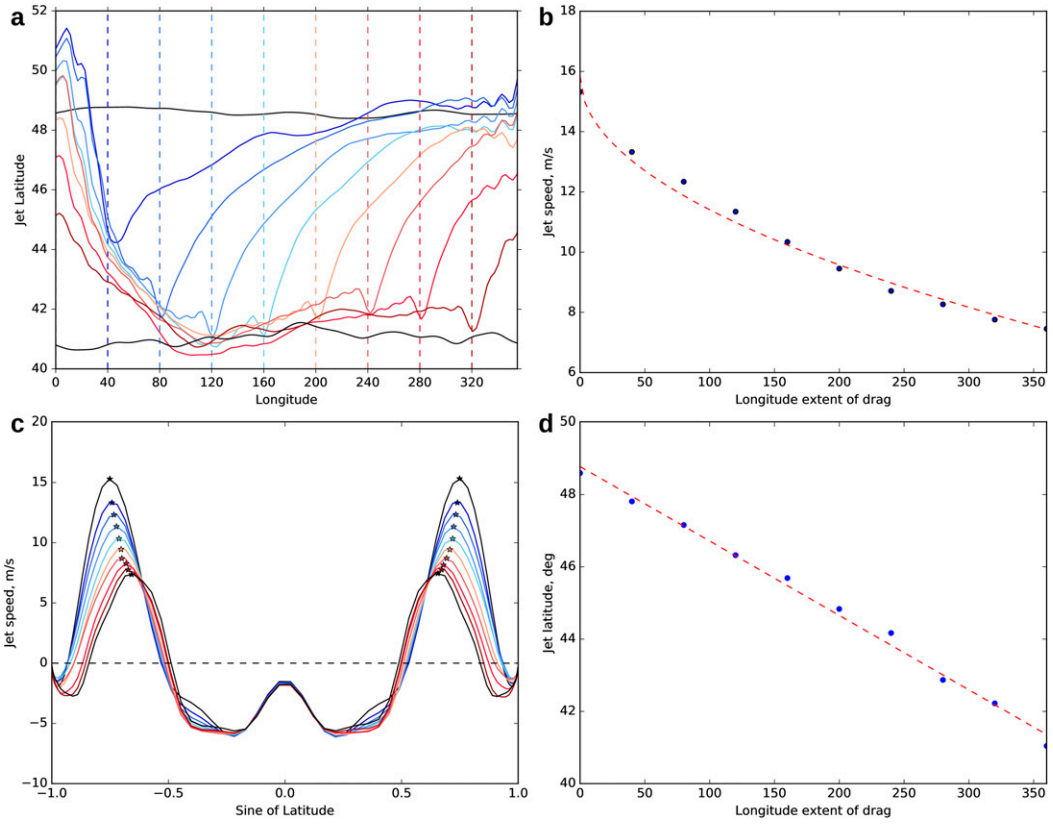


FIG. 12. (a) Longitude profiles of the extremum of the near-surface zonal wind (i.e., the jet axis) for simulations in which the longitudinal extent of the near-surface drag within the baroclinic zone is enhanced relative to the rest of the globe. The dashed vertical lines denote the drag extent for jet axis profiles of the same color. The black lines show the no-enhancement and the axisymmetric-enhancement cases. (b) The zonal-mean jet speed response to increases in the longitudinal extent of near-surface drag. The dashed red curve shows a nonlinear fit to the GCM's output. (c) The near-surface zonal-mean zonal wind profile response to changes in the longitudinal extent of near-surface baroclinic-zone drag. The stars indicate the computed locations of the jet. (d) The zonal-mean jet latitude response to increases in the longitudinal extent of near-surface drag. The dashed red line shows a linear fit to the GCM's output.

Our results agree with prior work that suggests that eddy dynamics on the poleward flank of the jet are more important for the eddy-driven jet shift in response to changes in near-surface drag (Lorenz 2014), in contrast to the idea that subtropical dynamics are primarily responsible for the shift (Chen et al. 2007).

We find that the phase speeds of eddies with the largest near-surface heat flux are also the phase speeds at which upper-tropospheric eddies transport the largest amount of momentum. Poleward eddy heat fluxes—largely the product of baroclinic instability—are associated with upward fluxes of wave activity, which in turn excite upper-tropospheric, equatorward-propagating Rossby waves. These Rossby waves converge momentum into the region of their excitation. The similarity of phase speeds appears analogous to the frequency of the forcing equaling the frequency of the response in a simple forced harmonic system.

Because extrema in the near-surface heat flux spectra shift equatorward in tandem with the eddy-driven jet when drag is perturbed globally and in the baroclinic zone, it is possible that shifts in the baroclinic stirring explain the eddy-driven jet shift. Therefore, we hypothesize that changes in the baroclinic driving causally shifts the jets in our simulations.

The equinox, hemispherically asymmetric simulations (Fig. 8) show that changes in drag in one hemisphere are balanced by circulation responses in the forced hemisphere with relatively little extratropical response in the opposite hemisphere. This may be in contrast to simulations in moist climates in which moisture responses may enhance linkages between opposite hemispheres (Polichtchouk and Shepherd 2016).

The near-surface protrusion of westerlies into the tropics off the west coasts of North America and North Africa is caused by the land–sea friction contrast. Compare the

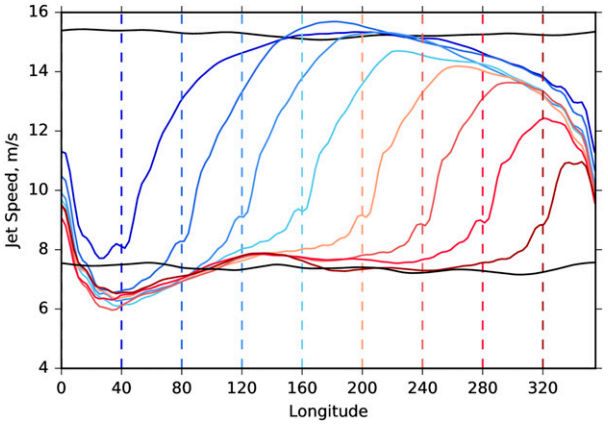


FIG. 13. Longitude profiles of the near-surface zonal wind speed along the jet axis for simulations in which the longitudinal extent of the near-surface drag within the baroclinic zone is enhanced relative to the rest of the globe. The dashed vertical lines denote the drag extents for the jet speed profiles of the same color. The black lines show the no-drag-enhancement and the axisymmetric-drag-enhancement cases.

contours in Figs. 10a and 10b to see this effect. This protrusion is important because it may facilitate Rossby wave propagation into midlatitudes. Waveguides are zonal bands of upper-level westerly winds. They enable meridional propagation of Rossby waves. Upper-level tropical divergences, forced, for example, by tropical convection, generate Rossby waves that could propagate into the extratropics along these waveguides and influence extratropical variability (Hoskins and Karoly 1981; Hoskins and Ambrizzi 1993; Ambrizzi and Hoskins 1997). One of the stationary responses to increases in near-surface drag (see Fig. 16) is a westerly wind anomaly on the equatorward flank of the continent. Furthermore, because surface drag is balanced by column-integrated eddy momentum flux convergences, enhanced near-surface drag forces eddy momentum flux convergences aloft and accelerates the westerlies. Thus, these two effects suggest that the surface drag associated with continents in the vicinity of the subtropics extends westerlies anomalously equatorward, shifting the waveguides closer to the regions of tropical convection. Hence, the subtropical continents could play an important role in tropical–extratropical teleconnections. This provides an additional reason why it is important for climate and forecast models to get the location and intensity of boundary layer drag correct.

Increasing drag over the oceans in the Northern Hemisphere leads to an eastward extension of the weakly localized Atlantic and Pacific jets. These localized jets occur on the western edge of the Pacific and Atlantic Oceans (contours in Fig. 10c), and the strongest jet shifts occur at the eastern edge of the enhanced drag region (Fig. 12a and Fig. 14) largely because of enhanced stationary-eddy fluxes (Fig. 16). The combined effect manifests as an extension of the eastern edge of the localized jet.

Increasing drag globally shifts the eddy-driven jet equatorward, in agreement with previous studies. It is also in agreement with the results from studies using the less realistic, Rayleigh friction parameterizations in their simulations (i.e., linear drag).

We find that despite the linear decrease in latitude of the zonal-mean jet maximum with increasing longitude extent of baroclinic zone drag, the zonal profile of wind in the sector drag experiments exhibits a rich structure and may even show a local poleward shift of the jet axis. Local near-surface drag was also found to influence the jet axis tilt.

The gradually increasing boundary layer drag in the meridional direction shifted the eddy-driven jet equatorward only after the drag reaches in the vicinity of the jet, yet, when the friction reached the jet, the equatorward jet shift was similar in magnitude to the shifts seen when drag was increased globally. Increasing the drag starting at the pole and moving toward the equator (not shown) also yields an abrupt transition when the drag reaches under the jet. Because a large proportion of the overall jet shift occurs when the boundary layer drag crosses under the jet, and because the response is independent of the direction from which the boundary layer drag approaches prior to crossing the jet, the principal mechanism controlling the jet shift is likely to be local in dry models.

The hemispherically asymmetric simulations show that variations in drag in one hemisphere have negligible effects in the opposite hemisphere. Therefore, and consistent with the interpretation of Polichtchouk and Shepherd (2016), moist dynamics and ocean dynamics likely account for any cross-equatorial effects observed in more complex models. Nonetheless, these results suggest that biases in the dry part of the dynamics may be addressed in a hemispherically independent way. That is, one can adjust drag in one hemisphere without adversely affecting the other through dry dynamical responses.

We showed that stationary eddies help localize extratropical storm tracks. This is not a new result (Chang et al. 2002; Kaspi and Schneider 2013). But here, localization is demonstrated in the absence of orography and diabatic heat sources. What is new is the natural extension of the results contained herein that suggests that the stationary eddies associated with a downstream continent help terminate an upstream storm track by creating an unfavorable meridional temperature gradient through stationary-eddy temperature fluxes (see Fig. 16). Hence, the European continent helps terminate the Atlantic storm track not only though stationary eddies generated

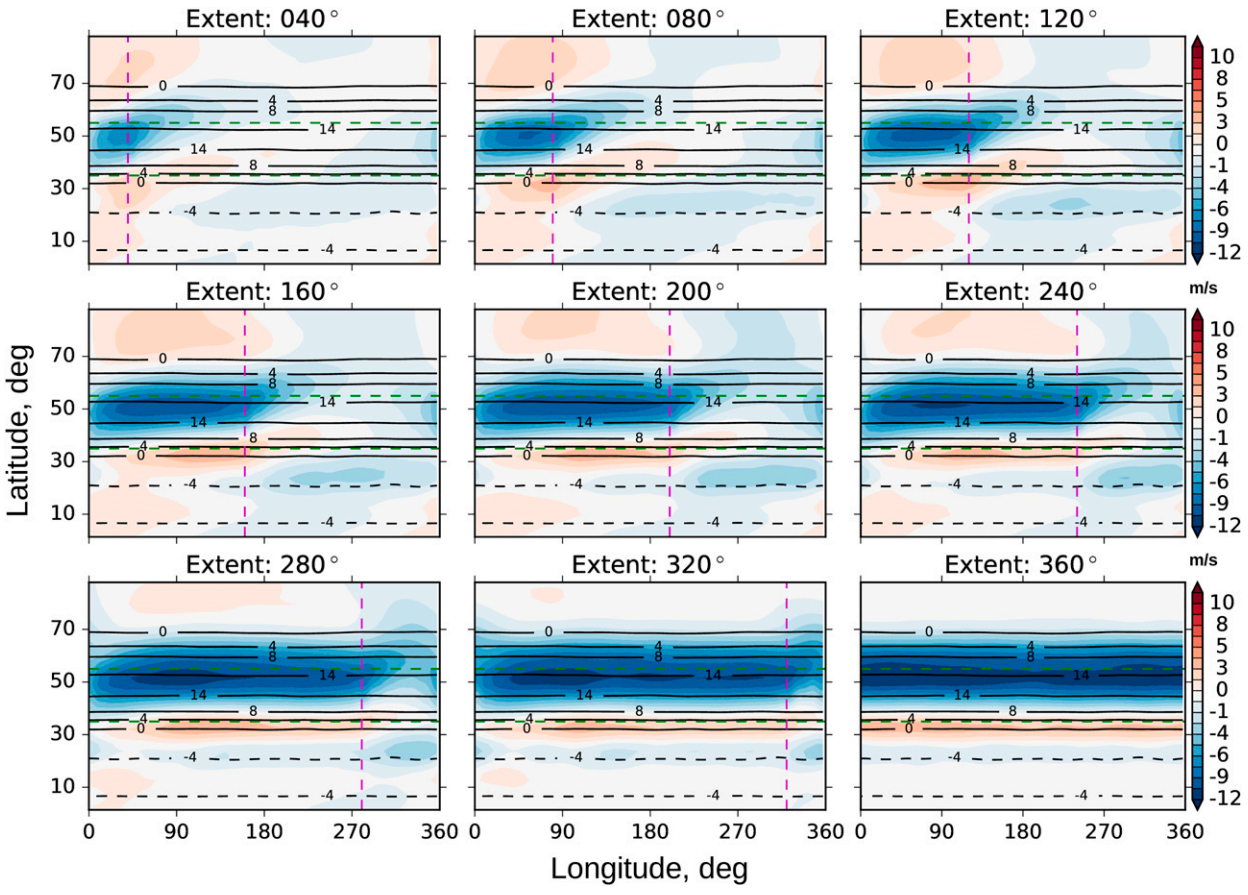


FIG. 14. Filled, colored contours indicate the zonal wind anomaly field for simulations in which drag is enhanced in the baroclinic zone relative to the unperturbed simulation (black, unfilled contours). The vertical magenta lines show the longitudinal extent of the enhanced drag in the baroclinic zone (the region between the dashed green lines). In all simulations, the enhanced near-surface drag starts at 0° longitude.

by the storm track itself (Kaspi and Schneider 2013), or from the direct mechanically forced dissipation (Chang et al. 2002), but also through the drag-induced stationary-wave fluxes associated with the continent. The same is true of the adverse effect of the American continent on the Pacific storm track. This result complements recent work, which finds that near-surface drag modulates circulation responses through stationary-wave interactions (van Niekerk et al. 2017).

### *Theory of eddy-driven jet shifts in response to boundary layer drag*

Drag, a nonconservative force, does negative work on a fluid parcel. Sources of drag in Earth's atmosphere include skin friction at the surface, form drag associated with a flow impinging on topography, and momentum transfer associated with macroturbulence and breaking waves. The applicable physical law is the conservation of angular momentum. The zonal angular momentum $l$ of a fluid parcel consists of two parts, the part due to Earth's solid-body rotation and the part due to the parcel's relative motion:

$$l = \Omega(a\cos\varphi)^2 + ua\cos\varphi, \tag{4}$$

where $a$ is the mean radius of Earth, $\varphi$ is latitude, and $\Omega$ is Earth's angular velocity.

#### 1) THE ANGULAR MOMENTUM–CONSERVING CASE

Insight into the expected shifts of tropospheric jets due to changes in zonal wind speed in a rotating frame can be obtained by considering the angular momentum–conserving case. It is apparent from Eq. (4) that $l = l(u, \varphi)$, if $a$ and $\Omega$ are considered parameters.

In the absence of torques on a system, $l$ is conserved, which implies that

$$\Delta l = 0 = \partial_u l \Delta u + \partial_\varphi l \Delta\varphi. \tag{5}$$

From Eq. (4), we have that $\partial_u l = a\cos\varphi$ and $\partial_\varphi l = -a\sin\varphi(2\Omega a\cos\varphi + u)$. In this angular momentum–conserving regime, a simple relation emerges for changes in

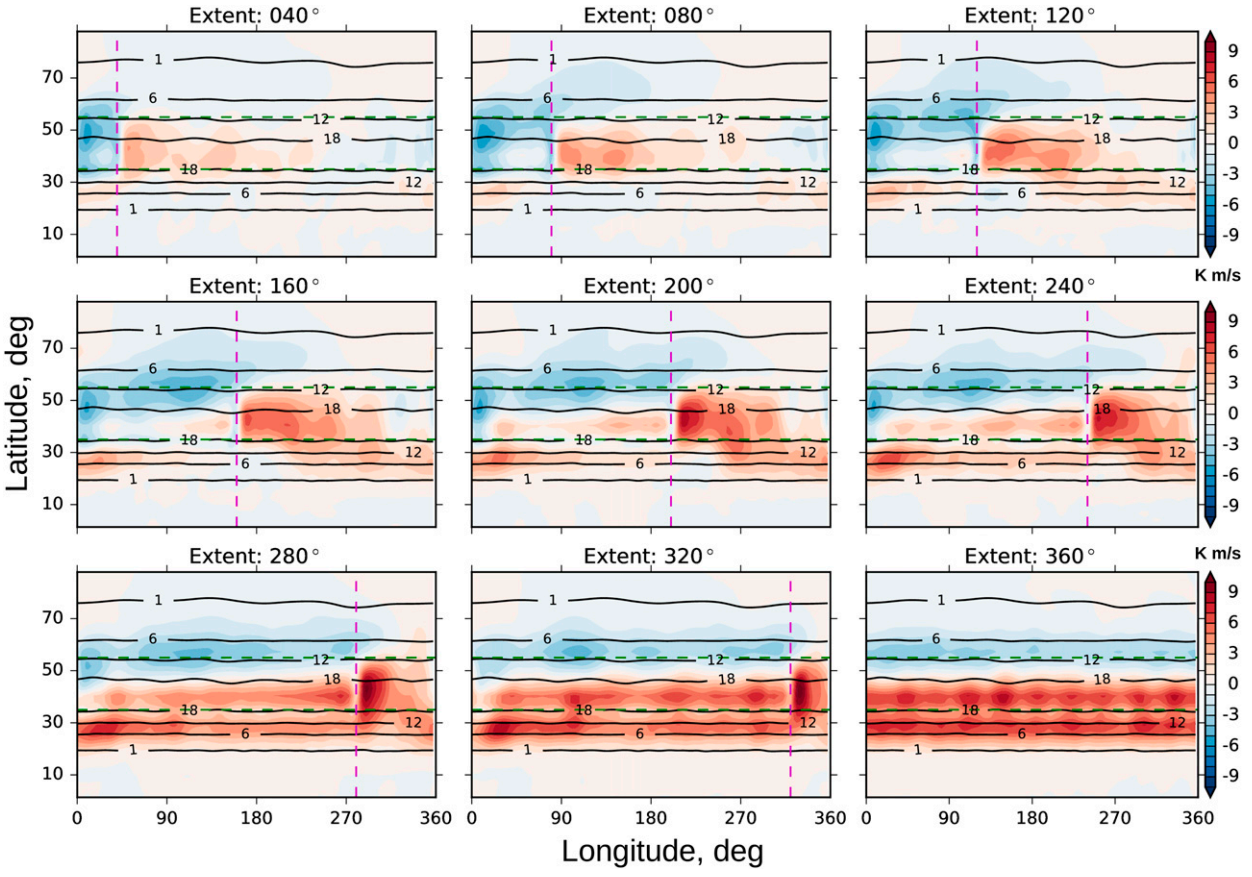


FIG. 15. As in Fig. 14, but for the field of near-surface meridional transient eddy temperature fluxes $\overline{v'T'}\cos\varphi$, where the overline represents a temporal mean, and the primes represent departures therefrom.

the latitude of a fluid parcel immediately following an externally forced change to its zonal wind speed:

$$\Delta\varphi = -\frac{\partial_u l}{\partial_\varphi l}\Delta u, \tag{6}$$

$$\Delta\varphi = \frac{\cot\varphi}{2\Omega a\cos\varphi + u}\Delta u. \tag{7}$$

Equation (7) suggests that a fluid parcel will shift poleward for externally forced increases in its zonal wind speed and equatorward for externally forced decreases in its zonal wind speed. Figure 17 shows the increase in a fluid parcel's latitude for a $1\,\mathrm{m\,s^{-1}}$ increase in its zonal wind speed, if it conserves its angular momentum. It is clear from the figure that the parcel's increase in latitude is everywhere directly proportional to the externally forced increase in zonal wind speed. However, the sensitivity to increases in zonal wind speed is a decreasing function of latitude. These results are consistent with our expectations because changes in angular momentum depend on changes in the perpendicular distance to Earth's axis of rotation and because larger changes in latitude are required at lower latitudes for equal changes in the perpendicular distance to Earth's axis of rotation than at higher latitudes. Whereas this simple analysis presents a useful indication of how the latitude of jets could change as the wind speed changes in the absence of torques on the fluid parcel, it is inadequate for explaining changes in the eddy-driven jet since drag plays an important role and since angular momentum is not conserved in midlatitudes in the presence of macroturbulence. Furthermore, the analysis predicts enhanced sensitivities on the equatorward flank of the jet, while our simulations show enhanced sensitivities on the poleward flank of the jet.

### 2) THE NONCONSERVATIVE FORCE CASE

Because the effects of surface drag are of interest, we start with the near-surface zonal-mean zonal momentum equation within the baroclinic zone:

$$f\overline{v} = \partial_y(\overline{u}\,\overline{v} + \overline{u'v'}) + \partial_p(\overline{u}\,\overline{w} + \overline{u'w'}), \tag{8}$$

where the overline represents a time and zonal mean, and the prime represents a departure from a temporal

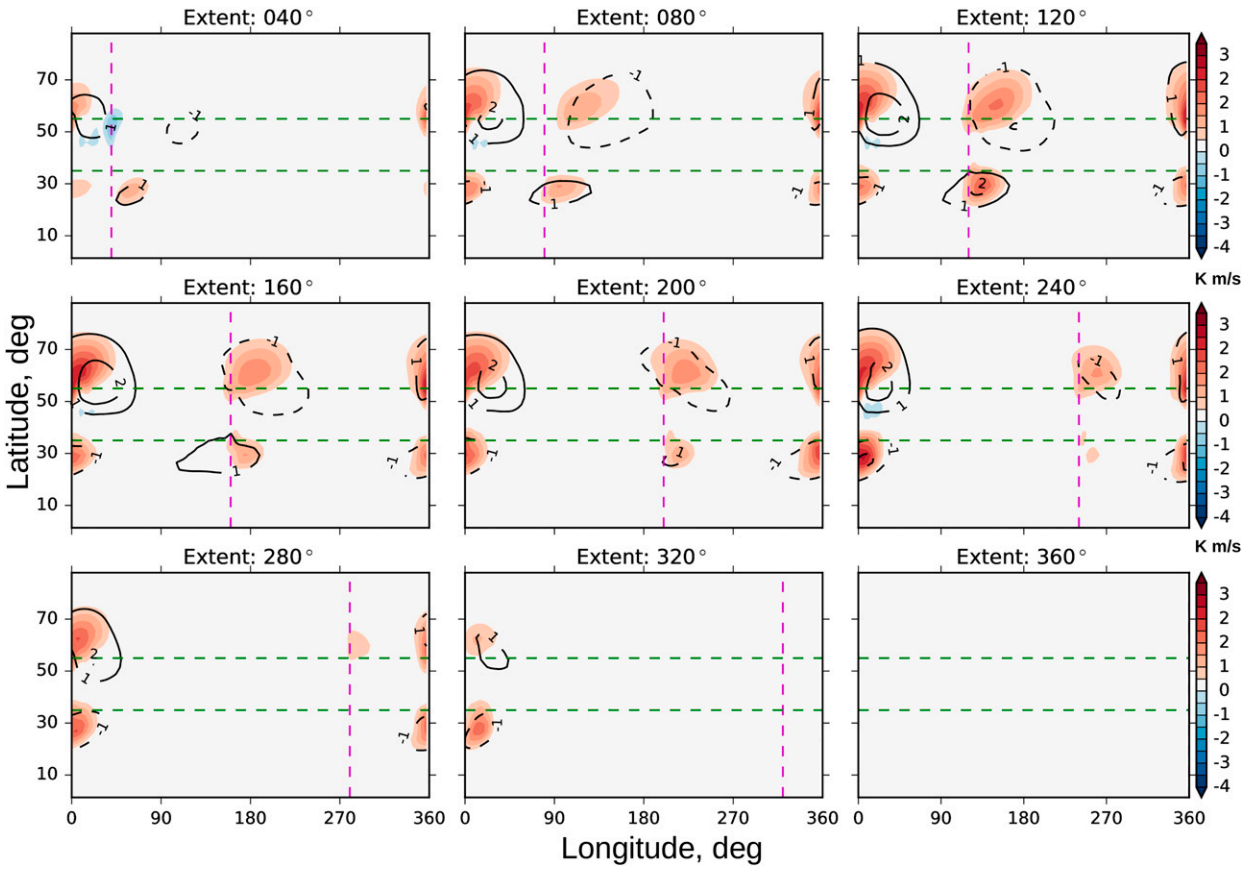


FIG. 16. As in Fig. 14, but for the field of near-surface meridional stationary-eddy temperature fluxes $\overline{v}^*\overline{T}^*\cos\varphi$ (color shading) and the near-surface stationary temperature anomaly $\overline{T}^*$ (black contours). The asterisks in these terms represent departures from a zonal mean.

mean. Near to the surface, the mean northward flux of westerly momentum by transient eddies is negligible (Ait-Chaalal and Schneider 2015; see also Fig. 4). Within the baroclinic zone, the mean meridional circulation is the thermally indirect, eddy-driven Ferrel cell. If, following Schneider and Bordoni (2008), one considers the interior of the baroclinic zone, where the surface streamlines are approximately horizontal, then one may neglect vertical momentum transports by the mean meridional circulation. Combined, these assumptions reduce the zonal momentum equation to

$$(1 - \mathrm{Ro})f\overline{v} = \tau\overline{u}, \tag{9}$$

where $\mathrm{Ro} = \partial_y\overline{u}/f$ is the local Rossby number. Here, we model near-surface vertical eddy momentum flux divergences as a linear drag, for expository purposes. Here $\tau^{-1}$ is the drag time scale.

The zonal-mean meridional momentum equation within the baroclinic zone is given by

$$-f\overline{u} - \partial_y\overline{\Phi} = \partial_y(\overline{v}^2 + \overline{v'^2}) + \partial_p(\overline{v}\,\overline{w} + \overline{v'w'}), \tag{10}$$

where $\overline{\Phi}$ is the time and zonal-mean geopotential. Similarly, the zonal-mean meridional momentum equation reduces to

$$(1 - \mathrm{Ro})f\overline{u} = -\tau\overline{v} - \partial_y\overline{B}, \tag{11}$$

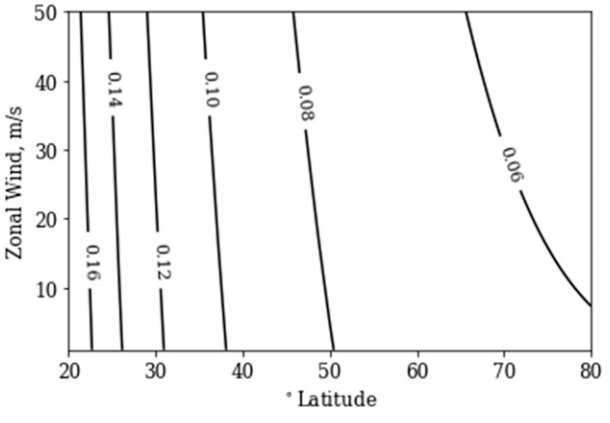


FIG. 17. The sensitivity of a fluid parcel's latitude to an externally forced change in its zonal wind speed under the assumption of angular momentum conservation. The numbers show the change in latitude assuming a 1 m s$^{-1}$ change in the zonal-mean zonal wind speed.

where $B = \overline{\Phi} + 0.5(\overline{u}^2 + \overline{v}^2)$ is the Bernoulli function. Hence, we have a system of equations [Eqs. (9) and (11)] that we solve, treating the gradient of the Bernoulli function as a parameter:

$$\overline{u} = -\frac{(1 - \mathrm{Ro}) f \partial_y \overline{B}}{f^2 (1 - \mathrm{Ro})^2 + \tau^2}, \tag{12}$$

$$\overline{v} = -\frac{\tau \partial_y \overline{B}}{f^2 (1 - \mathrm{Ro})^2 + \tau^2}. \tag{13}$$

We note that these equations are the same ones derived in Schneider and Bordoni (2008). The partial derivative of the equations of $\overline{u}$ and $\overline{v}$ gives one measure of the sensitivity of the zonal-mean winds to linear drag. The sensitivities can be used to ascertain whether the asymmetries in the zonal-mean wind's response to changes in drag result from the zonal profile of the components of the sensitivities. The drag sensitivities are found to be

$$\delta \overline{u}_\tau = \partial_y \overline{B} \frac{2\tau f (1 - \mathrm{Ro})}{\left[f^2 (1 - \mathrm{Ro})^2 + \tau^2\right]^2} \delta\tau, \tag{14}$$

$$\delta \overline{v}_\tau = -\partial_y \overline{B} \frac{f^2 (1 - \mathrm{Ro})^2 - \tau^2}{\left[f^2 (1 - \mathrm{Ro})^2 + \tau^2\right]^2} \delta\tau. \tag{15}$$

First, observe that the limit of the sensitivities as the Coriolis parameter gets large is zero. Bearing in mind that in midlatitudes $\mathrm{Ro} \ll 1$, it becomes clear that Earth's curvature does not explain the enhanced reduction of $\overline{u}$ on the poleward flank of the jet as drag increases uniformly in the baroclinic zone. Indeed, because $f$ is a monotonically increasing function of latitude and because the sensitivities are inversely proportional to $f$, higher latitudes will experience lower sensitivities to changes in drag, which is contrary to our observations.

Since the near-surface drag in our simulations is a constant function of latitude within the baroclinic zone, we turn our attention to the zonal-mean meridional profile of the Bernoulli function. Figure 18 plots the Bernoulli function and its components for the control simulation. The gradient of the Bernoulli function is predominantly negative and dominated by the geopotential term. The geopotential gradient is asymmetric about the jet core: it is less negative on the equatorward flank of the jet. The mean kinetic energy gradient is also asymmetric about the jet maximum; it changes sign. The sense of these asymmetries enhances the sensitivity of the zonal-mean zonal wind to changes in near-surface drag on the poleward flank of the jet, while it reduces the sensitivity on the equatorward flank. Indeed, the meridional profile of drag sensitivity, which

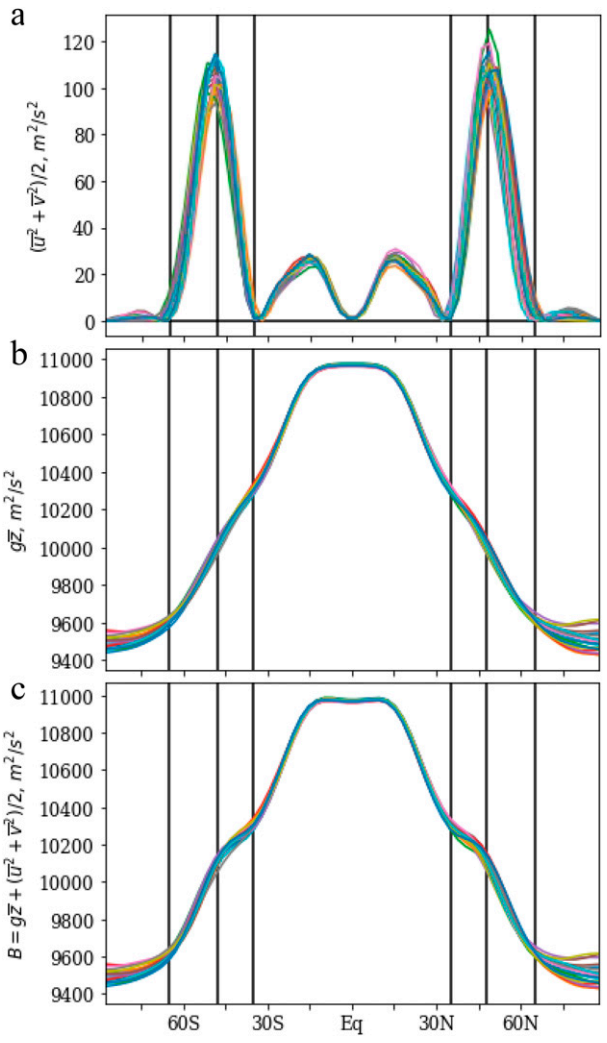


FIG. 18. Zonal-mean profiles of (c) the Bernoulli function and its components [(a) mean kinetic energy and (b) geopotential], computed for the control simulation, which has no enhanced drag. The profiles are computed using near-surface vertical averages between $\sigma = 0.84$ and $\sigma = 0.93$. Each colored line represents a 90-day average over the control simulation, which is in a statistically steady state and has been spun up for 1800 days. The black vertical lines bound the baroclinic zone and mark the eddy-driven jet maximum.

is dominated by the Bernoulli function, explains why the jet response to changes in drag is asymmetric about the jet core. The sensitivities associated with the gradient in the mean kinetic energy enhances the asymmetry in the sensitivity, but it is secondary to the asymmetry associated with the gradient of the geopotential.

Therefore, the equatorward shift in the eddy-driven jet results from a contraction on the poleward flank of the baroclinic zone. The contraction on the poleward flank of the jet may sometimes be accompanied by an equatorward jet expansion. These changes in the baroclinic zone are driven primarily by the profile of the

Bernoulli function, which is asymmetric about the storm tracks and eddy-driven jet.

## 5. Conclusions

Novel simulations were conducted in a dry, idealized general circulation model (GCM). These simulations provide new insight into the eddy-driven jet dynamics in response to changes in near-surface drag and a new, rich array of case studies against which to test theories of jet and storm-track shifts.

By perturbing the near-surface drag in a zonal band in the vicinity of the eddy-driven jet, we demonstrated that much of the jet response to global variations in surface drag are captured by perturbing the drag locally about the climatological jet.

Hemispherically asymmetric near-surface drag simulations were conducted to probe possible interhemispheric dynamical interactions. However, it was found that perturbing drag in one hemisphere had negligible effect on the eddy-driven jet in the opposite hemisphere. This remained true when the simulations were run in perpetual summer and winter configurations. This suggests that it is possible to adjust drag in one hemisphere without substantially affecting the jet in the opposite hemisphere through dry dynamics.

The eddy-driven jet latitude was found to be more sensitive to variations in near-surface drag in summer than in winter; while the wintertime eddy-driven jet strength was more sensitive to perturbations in near-surface drag. It was shown that there was a larger change in jet speed in winter because the jet speeds are higher in winter. Furthermore, it was shown that asymmetries in the Bernoulli function explain the asymmetric reduction in the jet speed around the core, which resulted in an equatorward contraction of the jet when near-surface drag increases.

It is found that zonally localized drag sets up a localized storm track and a tilted jet downstream. Furthermore, it was demonstrated that differential variations in land versus ocean drag can modify the tilt of the Atlantic and Pacific jets.

Finally, it is suggested that the near-surface drag associated with Earthlike continents facilitates tropical–extratropical teleconnections by modifying subtropical waveguides. Thus, climate and forecast models have additional reasons to better constrain their drag parameterizations, especially in the subtropics and extratropics.

The results contained herein demonstrate that further research into the fundamentals of eddy-driven jet dynamics is warranted and that scope exists for advancing our understanding of it in order to improve climate and forecast models.

*Acknowledgments.* This work was conducted as part of the summerTIME project and was funded through the NERC Grant NE/M005887/1. We thank the reviewers for their helpful comments on the original manuscript.

## REFERENCES

Ait-Chaalal, F., and T. Schneider, 2015: Why eddy momentum fluxes are concentrated in the upper troposphere. *J. Atmos. Sci.*, **72**, 1585–1604, https://doi.org/10.1175/JAS-D-14-0243.1.

Ambrizzi, T., and B. J. Hoskins, 1997: Stationary Rossby-wave propagation in a baroclinic atmosphere. *Quart. J. Roy. Meteor. Soc.*, **123**, 919–928, https://doi.org/10.1002/qj.49712354007.

Baker, H. S., T. Woollings, and C. Mbengue, 2017: Eddy-driven jet sensitivity to diabatic heating in an idealized GCM. *J. Climate*, **30**, 6413–6431, https://doi.org/10.1175/JCLI-D-16-0864.1.

Barnes, E. A., and D. L. Hartmann, 2011: Rossby wave scales, propagation, and the variability of eddy-driven jets. *J. Atmos. Sci.*, **68**, 2893–2908, https://doi.org/10.1175/JAS-D-11-039.1.

——, ——, D. M. W. Frierson, and J. Kidston, 2010: Effect of latitude on the persistence of eddy-driven jets. *Geophys. Res. Lett.*, **37**, L11804, https://doi.org/10.1029/2010GL043199.

Brayshaw, D. J., B. Hoskins, and M. Blackburn, 2008: The storm-track response to idealized SST perturbations in an aquaplanet GCM. *J. Atmos. Sci.*, **65**, 2842–2860, https://doi.org/10.1175/2008JAS2657.1.

——, ——, and ——, 2009: The basic ingredients of the North Atlantic storm track. Part I: Land–sea contrast and orography. *J. Atmos. Sci.*, **66**, 2539–2558, https://doi.org/10.1175/2009JAS3078.1.

Chang, E., S. Lee, and K. Swanson, 2002: Storm track dynamics. *J. Climate*, **15**, 2163–2183, https://doi.org/10.1175/1520-0442(2002)015<02163:STD>2.0.CO;2.

Charney, J. G., 1947: The dynamics of long waves in a baroclinic westerly current. *J. Meteor.*, **4**, 135–162, https://doi.org/10.1175/1520-0469(1947)004<0136:TDOLWI>2.0.CO;2.

Chen, G., I. M. Held, and W. A. Robinson, 2007: Sensitivity of the latitude of the surface westerlies to surface friction. *J. Atmos. Sci.*, **64**, 2899–2915, https://doi.org/10.1175/JAS3995.1.

Eady, E. T., 1949: Long waves and cyclone waves. *Tellus*, **1** (3), 33–52, https://doi.org/10.3402/tellusa.v1i3.8507.

Hayashi, Y., 1971: A generalized method of resolving disturbances into progressive and retrogressive waves by space Fourier and time cross-spectral analysis. *J. Meteor. Soc. Japan*, **49**, 125–128, https://doi.org/10.2151/jmsj1965.49.2_125.

Held, I. M., and M. J. Suarez, 1994: A proposal for the intercomparison of the dynamical cores of atmospheric general circulation models. *Bull. Amer. Meteor. Soc.*, **75**, 1825–1830, https://doi.org/10.1175/1520-0477(1994)075<1825:APFTIO>2.0.CO;2.

Hoskins, B. J., and D. J. Karoly, 1981: The steady linear response of a spherical atmosphere to thermal and orographic forcing. *J. Atmos. Sci.*, **38**, 1179–1196, https://doi.org/10.1175/1520-0469(1981)038<1179:TSLROA>2.0.CO;2.

——, and T. Ambrizzi, 1993: Rossby wave propagation on a realistic longitudinally varying flow. *J. Atmos. Sci.*, **50**, 1661–1671, https://doi.org/10.1175/1520-0469(1993)050<1661:RWPOAR>2.0.CO;2.

James, I. N., 1987: Suppression of baroclinic instability in horizontally sheared flows. *J. Atmos. Sci.*, **44**, 3710–3720, https://doi.org/10.1175/1520-0469(1987)044<3710:SOBIIH>2.0.CO;2.

——, and L. J. Gray, 1986: Concerning the effect of surface drag on the circulation of a baroclinic planetary atmosphere.

*Quart. J. Roy. Meteor. Soc.*, **112**, 1231–1250, https://doi.org/10.1002/qj.49711247417.

Kaspi, Y., and T. Schneider, 2013: The role of stationary eddies in shaping midlatitude storm tracks. *J. Atmos. Sci.*, **70**, 2596–2613, https://doi.org/10.1175/JAS-D-12-082.1.

Kidston, J., and G. K. Vallis, 2010: Relationship between eddy-driven jet latitude and width. *Geophys. Res. Lett.*, **37**, L21809, https://doi.org/10.1029/2010GL044849.

——, and ——, 2012: The relationship between the speed and the latitude of an eddy-driven jet in a stirred barotropic model. *J. Atmos. Sci.*, **69**, 3251–3263, https://doi.org/10.1175/JAS-D-11-0300.1.

Lorenz, D. J., 2014: Understanding midlatitude jet variability and change using Rossby wave chromatography: Wave–mean flow interaction. *J. Atmos. Sci.*, **71**, 3684–3705, https://doi.org/10.1175/JAS-D-13-0201.1.

Lorenz, E., 1955: Available potential energy and the maintenance of the general circulation. *Tellus*, **7**, 157–167, https://doi.org/10.3402/tellusa.v7i2.8796.

Mbengue, C., and T. Schneider, 2013: Storm track shifts under climate change: What can be learned from large-scale dry dynamics. *J. Climate*, **26**, 9923–9930, https://doi.org/10.1175/JCLI-D-13-00404.1.

——, and ——, 2017: Storm-track shifts under climate change: Toward a mechanistic understanding using baroclinic mean available potential energy. *J. Atmos. Sci.*, **74**, 93–110, https://doi.org/10.1175/JAS-D-15-0267.1.

——, and ——, 2018: Linking Hadley circulation and storm tracks in a conceptual model of the atmospheric energy balance. *J. Atmos. Sci.*, **75**, 841–856, https://doi.org/10.1175/JAS-D-17-0098.1.

Phillips, N., 1956: The general circulation of the atmosphere: A numerical experiment. *Quart. J. Roy. Meteor. Soc.*, **82**, 123–164, https://doi.org/10.1002/qj.49708235202.

Pithan, F., T. G. Shepherd, G. Zappa, and I. Sandu, 2016: Climate model biases in jet streams, blocking and storm tracks resulting from missing orographic drag. *Geophys. Res. Lett.*, **43**, 7231–7240, https://doi.org/10.1002/2016GL069551.

Polichtchouk, I., and T. G. Shepherd, 2016: Zonal-mean circulation response to reduced air–sea momentum roughness. *Quart. J. Roy. Meteor. Soc.*, **142**, 2611–2622, https://doi.org/10.1002/qj.2850.

Randel, W. J., and I. M. Held, 1991: Phase speed spectra of transient eddy fluxes and critical layer absorption. *J. Atmos. Sci.*, **48**, 688–697, https://doi.org/10.1175/1520-0469(1991)048<0688:PSSOTE>2.0.CO;2.

Robinson, W. A., 1997: Dissipation dependence of the jet latitude. *J. Climate*, **10**, 176–182, https://doi.org/10.1175/1520-0442(1997)010<0176:DDOTJL>2.0.CO;2.

——, 2000: A baroclinic mechanism for the eddy feedback on the zonal index. *J. Atmos. Sci.*, **57**, 415–422, https://doi.org/10.1175/1520-0469(2000)057<0415:ABMFTE>2.0.CO;2.

Sandu, I., P. Bechtold, A. Beljaars, A. Bozzo, F. Pithan, T. G. Shepherd, and A. Zadra, 2016: Impacts of parameterized orographic drag on the Northern Hemisphere winter circulation. *J. Adv. Model. Earth Syst.*, **8**, 196–211, https://doi.org/10.1002/2015MS000564.

Schneider, T., 2004: The tropopause and the thermal stratification in the extratropics of a dry atmosphere. *J. Atmos. Sci.*, **61**, 1317–1340, https://doi.org/10.1175/1520-0469(2004)061<1317:TTATTS>2.0.CO;2.

——, and C. Walker, 2006: Self-organization of atmospheric macroturbulence into critical states of weak nonlinear eddy–eddy interactions. *J. Atmos. Sci.*, **63**, 1569–1586, https://doi.org/10.1175/JAS3699.1.

——, and S. Bordoni, 2008: Eddy-mediated regime transitions in the seasonal cycle of a Hadley circulation and implications for monsoon dynamics. *J. Atmos. Sci.*, **65**, 915–934, https://doi.org/10.1175/2007JAS2415.1.

Stephenson, D. B., 1994: The Northern Hemisphere tropospheric response to changes in the gravity-wave drag scheme in a perpetual January GCM. *Quart. J. Roy. Meteor. Soc.*, **120**, 699–712, https://doi.org/10.1002/qj.49712051709.

——, 1995: The impact of changing the horizontal diffusion scheme on the northern winter climatology of a general circulation model. *Quart. J. Roy. Meteor. Soc.*, **121**, 211–226, https://doi.org/10.1002/qj.49712152110.

van Niekerk, A., J. F. Scinocca, and T. G. Shepherd, 2017: The modulation of stationary waves, and their response to climate change, by parameterized orographic drag. *J. Atmos. Sci.*, **74**, 2557–2574, https://doi.org/10.1175/JAS-D-17-0085.1.

Woollings, T., A. Hannachi, and B. Hoskins, 2010: Variability of the North Atlantic eddy-driven jet stream. *Quart. J. Roy. Meteor. Soc.*, **136**, 856–868, https://doi.org/10.1002/qj.625.

Yin, J. H., 2005: A consistent poleward shift of the storm tracks in simulations of 21st century climate. *Geophys. Res. Lett.*, **32**, L18701, https://doi.org/10.1029/2005GL023684.